EUROPEAN ORGANIZATION FOR NUCLEAR RESEARCH

COHERENT PRODUCTION OF LOW-MASS $p\pi^+\pi^-$ STATES IN THE INTERACTION OF 18.6 GeV/c PROTONS WITH ^{4}He NUCLEI

T. Ekelöf*) and A.J. Herz

CERN, Geneva, Switzerland

E. Hagberg and S. Kullander

The Gustaf Werner Institute, Uppsala, Sweden

P.C. Bruton, J.K. Davies**), S.M. Fisher†), F.F. Heymann,

D.C. Imrie, G.J. Lush and J. Nassalski††)

Department of Physics and Astronomy, University College London,
London, England

ABSTRACT

A specially developed scintillator and spark chamber spectrometer has been used to measure recoiling ^{4}He target nuclei, and a magnetic spark chamber spectrometer to measure forward-going $p\pi^+\pi^-$ particles, selecting coherent events by four-momentum balance. Two enhancements in the $p\pi^+\pi^-$ mass spectrum are found at 1.49 and 1.71 GeV/c^2. The branching ratio of the quasi-two-body state $\Delta^{++}\pi^-$ is 42 ± 8% in the 1.71 GeV/c^2 mass region. The t slope, as a function of $p\pi^+\pi^-$ mass, is consistent with what can be predicted using the impulse approximation. The decay angular analysis indicates the presence of several interfering states in the 1.5 GeV/c^2 mass region and of one state of spin $\geq 3/2$, possibly $5/2$, in the 1.7 GeV/c^2 mass region. There is some preference shown for t-channel helicity conservation. The data are very similar to results obtained with proton targets, which provides independent support for the hypothesis that vacuum exchange is dominant in the production of low mass $p\pi^+\pi^-$ states in pp interactions around 20 GeV/c.

Geneva - 1 September 1977

(Submitted to Nuclear Physics B)

---

*) Now at the Gustaf Werner Institute, Uppsala, Sweden.
**) Now at Oxford University, England.
†) Now at the Rutherford Laboratory, Chilton, England.
††) Now at Institute for Nuclear Research, Warsaw, Poland.

1. INTRODUCTION

One of the interesting features of coherent production on nuclear targets by comparison with production on proton targets is the suppression of non-zero isospin exchange. This suppression is complete in the case of an isospin zero nucleus such as ^{4}He. The produced system must therefore have the same isospin as the incident proton, i.e. $\frac{1}{2}$, in contrast to $p\pi^+\pi^-$ production from a hydrogen target, in which case the produced system may have both isospin $\frac{1}{2}$ and $\frac{3}{2}$. A favourable feature of the ^{4}He nucleus is that all its excited states decay via particle emission. As a consequence, the identification of the ^{4}He nucleus after the collision is enough to ensure that the target remained in its ground state during the collision, i.e. that the production process was coherent. The ^{4}He particle also has the advantage of having a sufficiently low specific ionization to be detectable in the interesting momentum range with more or less conventional counter techniques.

In the present experiment, which was carried out at the CERN Proton Synchrotron (PS), a specially developed helium recoil spectrometer [1], containing scintillators and wire spark chambers, was used to detect the alpha particle emerging from the target. The $p\pi^+\pi^-$ system produced in the forward direction was detected in a large-aperture magnetic spark chamber spectrometer. The coherent $p^4\text{He} \rightarrow$ $\rightarrow p\pi^+\pi^-{}^4\text{He}$ events were selected from the incoherent background using the four constraints from momentum-energy conservation.

The main aim of the experiment was to look for features in the distributions of mass and angles of the produced $p\pi^+\pi^-$ system, which could originate from the fact that the $p\pi^+\pi^-$ system was produced only by isospin zero exchange.

2. APPARATUS

A plan view of the experimental apparatus is shown in Fig. 1.

An 18.6 GeV/c, unseparated, positive beam with a useful intensity of 10^5 protons per 400 msec burst was used. The momentum spread was ±0.5% FWHM. The image at the target was 8 mm wide × 4 mm high and the maximum horizontal and vertical

divergences were ±2.7 and ±5.4 mrad, respectively. The background of positive particles, other than protons, in the beam was measured to be well below 1%.

Ten planes of multiwire proportional chambers [2] (MWPC) in two blocks, 2.5 m apart, were used to measure incoming trajectories. Each block consisted of two planes with horizontal wires, two with vertical wires, and one with wires at 30° to the vertical. Each plane contained 48 signal wires at 2 mm spacing. Planes with parallel wires were displaced 1 mm laterally with respect to one another, to improve the spatial resolution of the system. The angular resolution was ±0.3 mrad in both the horizontal and the vertical plane. The average efficiency of a MWPC plane was measured to be 97.5%. The inefficiency of 2.5% was accounted for by the 500 nsec dead-time of the delay employed in the read-out electronics.

2.1 The helium recoil spectrometer

The helium recoil spectrometer contained a cylindrical, high-pressure ^{4}He gas target [3], 50 cm long by 2 cm diameter, two cylindrical spark chambers, coaxial with the target, and an outer ring of seven scintillation counters, which covered, in total, 7/8 of the azimuth. The complete spectrometer was mounted in a large, light-tight box, approximately 1 m long 1 m in diameter, containing a mixture of 82% helium and 18% ethyl alcohol at an absolute pressure of 6 kPa. The beam entered through an aluminium window 0.1 mm thick, and the rear of the spectrometer was provided with a second 0.5 mm thick aluminium window, 25 cm in diameter, which was reduced to a thickness of 0.1 mm in the beam region.

The target wall was fabricated from kapton sheeting, either 8 μm or 27 μm thick, and was supported by an external 2 mm-pitch spiral formed from 0.1 mm diameter stainless-steel wire. The 8 μm wall targets were used with an internal pressure of 800 kPa of helium, the 27 μm wall targets with 1500 kPa. The resulting minimum values of the four-momentum transfer to a helium nucleus from an interaction on the target axis were 0.05 and 0.07 $(GeV/c)^2$, respectively.

The electrodes of the cylindrical spark chambers were made of wires spaced 2 mm apart, attached at their ends to printed-circuit boards connected to

ring-shaped spacers of cast epoxy-resin. The small chamber had an inner radius of 13 cm and the large one an inner radius of 32 cm. In both chambers the gap between the high voltage and ground electrodes was 4 cm. The inner electrode of the small chamber and the outer electrode of the large one were constructed of stainless-steel wires of 70 μm diameter; the other two electrodes were constructed of 50 μm diameter gold-plated molybdenum. The spark coordinates were read out using both the current division method [4] and the lumped delay-line method [5]. An important advantage of the delay line read-out was that, provided there was a single spark in a chamber, the sum of the times of the pulses arriving at each end of a delay line was constant to within ±0.2%. Events with more than one spark in each chamber could thus be rejected using this sum as criterion. The standard measurement errors were 10 mm in the longitudinal coordinate and 6 mrad in the azimuthal angle. Each time the spark chambers were pulsed, 200 msec were needed for the chambers to recover. This time constituted the principal limitation on the data rate in the experiment.

The seven scintillation counters had a length of 50 cm and a thickness of 4 mm and were curved to form the surface of a cylinder of radius 37 cm. Strip light-guides connected the ends of each scintillator to 56 DVP photomultipliers. Signals were taken from the photomultiplier anodes for triggering purposes and analogue signals from the 11^{th} and 13^{th} dynodes for pulse-height analysis. Two analogue signals were necessary because of the large dynamic range, $\sim$ 1:150, produced by alpha particles with energies between 1 and 50 MeV stopping in the scintillator. In addition, the time of flight of the recoil particle was measured by recording the time difference between a pulse from the counter B4 in the incident beam and the anode pulses from each tube of the struck recoil scintillator.

The details of the helium recoil spectrometer have been described elsewhere [1].

2.2 The forward spectrometer

The forward spectrometer consisted of two blocks of magnetostrictive read-out spark chambers on each side of a large-aperture magnet. Downstream of the second

block of spark chambers there was a 32-element counter hodoscope, two beam veto counters, and two multi-cell atmospheric-pressure, threshold Čerenkov counters (see Fig. 1).

The two spark chamber blocks contained 24 planes of chambers each. The upstream block had eight planes with horizontal wires, eight with vertical wires, and eight with wires at ±45° to the vertical. The downstream block contained twelve planes with vertical wires and twelve with wires at ±30° to the vertical. Up to seven coordinates, including two fiducials, could be digitized from each spark chamber plane. The magnet had a useful aperture of 154 × 47 cm, a central field of 1.5 T, and a field integral of 1.98 Tm along the beam axis. The momentum resolution of the spectrometer was ±0.4% at 3 GeV/c and ±1.5% at 18 GeV/c.

The counter hodoscope, which was employed in the trigger to select the forward particle multiplicity, contained 32 scintillator strips, E1-E32, each 110 cm × 10 cm × 1 cm thick, viewed at each end by a photomultiplier. The two beam veto counters D1 and D2 were squares of 17 cm and 7.5 cm side, respectively.

The upstream threshold Čerenkov counter contained 14 cells, 7 above and 7 below the median plane. It was filled with freon-12, giving a threshold of approximately 20 GeV/c for protons, 10 GeV/c for kaons, and 3 GeV/c for pions. The second counter, which had 8 cells, 4 above and 4 below the median plane, was filled with nitrogen and had a threshold of approximately 20 GeV/c for kaons and 6 GeV/c for pions.

In order to eliminate accidental beam tracks which were recorded by the spark chambers, a system of seven MWPC planes [2], each containing 240 signal wires at 2 mm spacing, was installed between the recoil spectrometer and the forward spectrometer. Three of the planes had horizontal wires and four had wires at 45° to the vertical.

In order to facilitate triggering on multiparticle final states, four square scintillation counters, Q1-Q4, each with a quadrant cut from one corner, were arranged to form a plane array with a circular hole 25 mm in diameter, through

which the beam could pass. Finally, four large lead-loaded counters F1-F4 were arranged in the middle of the upstream block of spark chambers and used to define a rectangular aperture which just matched the acceptance of the spectrometer magnet.

The details of the major components of the forward spectrometer have been described elsewhere [6].

2.3 Trigger logic and computer control

Events with one, two, or three charged tracks traversing the forward spectrometer were collected concurrently. The complete event trigger was BEAM·$\overline{D2}$·ALPHA·(1P + 3P), where BEAM ≡ B1·B2·B3·B4·$\overline{V1}$·$\overline{V2}$·$\overline{V3}$·$(\overline{B1 \cdot B2})_{DEL}$. The scintillator B1 counted essentially all particles emerging from the last quadrupole and B2 all particles emerging from the last bending magnet of the beam transport system. B3 defined a central core of the beam, 27.5 mm in diameter, just downstream of B2; and B4, 13 mm in diameter, was situated just upstream of the helium gas target. V1 and V2, with central holes of diameter 15 mm and 12 mm, respectively, vetoed interactions occurring in B4 and in the entrance window of the recoil spectrometer. V3 vetoes beam particles which were accompanied by a halo particle within ±50 nsec. $(\overline{B1 \cdot B2})_{DEL}$ was a pile-up rejection signal, which vetoed beam tracks if there had been another beam particle within the preceding 230 nsec. $\overline{D2}$ indicates a veto signal derived from the smaller of the beam veto counters, and ALPHA is a signal from one of the scintillators of the recoil spectrometer. The coincidence of the signals from the beam and the forward-going fast particles was delayed electronically to be in coincidence with the recoil signal, which arrived late because of the comparatively long time of flight of the recoil particle. The time window of the delay was such that only events with a four-momentum transfer squared smaller than 0.18 $(GeV/c)^2$ were accepted. This trigger condition was important since it excluded high level background due to prompt coincidences from relativistic particles in the recoil scintillators.

1P and 3P indicate "one-prong" and "three-prong" trigger conditions, respectively. They were defined by

$$1P \equiv Q_1 \cdot E_1 \cdot \overline{D1}$$

and

$$3P \equiv Q_{\geq 2} \cdot (E_{\geq 2} \cdot \overline{F}_{\geq 2} + E_{\geq 3} \cdot \overline{F}_{\geq 1}) \ ,$$

where Q_1 indicates a count in one and only one of the four Q counters, $Q_{\geq 2}$ indicates that at least two Q counters produced a signal, and a similar notation is used for the E and F counters; $\overline{D1}$ was a veto signal obtained from the larger of the beam veto counters.

The definition of the three-prong events allowed for the limited acceptance of the forward spectrometer. If the effective mass of the dissociation products of the incoming proton was large, it was possible for only two of the three forward tracks to traverse the magnet and for the other to intercept one of the F counters.

Signals from the threshold Čerenkov counters were not included in the event trigger, but were used in the off-line analysis of the data.

Two on-line computers were used to monitor and control the apparatus. The forward spectrometer was connected to a DEC PDP 9, and the recoil spectrometer and the multiwire proportional chambers to a Honeywell DDP 516. The two computers were connected via a CAMAC-CAMAC link and, during data taking, information from the DDP 516 was transmiteed to the PDP 9, which merged the transmitted data with incoming data from the forward spectrometer and wrote a single event record on to magnetic tape.

3. DATA ANALYSIS

We will report here on the analysis of the three-prong events. The analysis of the one-prong events is described in a separate paper [7]. Raw data were first converted to track coordinates and momenta and then analysed in three stages: geometrical analysis and fitting, kinematical fitting, and assignment of acceptance weights.

The geometry program chose the best track combinations linking up through the spectrometer magnet. Only two of the three tracks had to pass through the magnet to provide an acceptable event candidate. The tracks of the beam, the recoil and the forward particles, were then used in a least squares fit subject to the constraint of all tracks passing through a common vertex.

The coherent $p^4He \rightarrow {}^4He\ p\pi^+\pi^-$ (i) events were selected from the sample of three-prong events that passed the geometrical fit. Two kinds of background reactions were important: incoherent reactions, in which the ^4He nucleus disintegrated into lighter nuclei, and other coherent reactions with three charged tracks in the forward direction, such as $p^4He \rightarrow {}^4He\ p\pi^+\pi^-\pi^0$ (ii), and $p^4He \rightarrow {}^4He\ \pi^+\pi^+\pi^-n$ (iii). The selection of coherent events was made by assigning masses to each of the measured particles and fitting the data to the kinematical constraints of the $p^4He \rightarrow {}^4He\ p\pi^+\pi^-$ reaction. In order to extract most of the coherent events from the incoherent background, reactions (ii) and (iii) were also used as hypotheses when fitting. The fit to the reaction (i) has four constraints unless one of the forward tracks has no momentum measurement, in which case it has three constraints. The fits to reactions (ii) and (iii) both have one constraint.

For a coherent event it was required that at least one of the three reaction hypotheses fitted the data with a χ^2 probability greater than 1%. This was the case in 35% of the data. A further requirement was that the recoil energy obtained from the pulse-height measurement, E_{PH}, and that obtained from the time-of-flight measurement, E_{TOF}, assuming a ^4He recoil, agreed within ±2.5 standard deviations. The distribution of the quantity

$$\chi = (E_{PH} - E_{TOF})/\sqrt{\sigma^2_{E_{PH}} + \sigma^2_{E_{TOF}}}$$

for fitted coherent events is shown in Fig. 2. The number of events outside the imposed limits is quite small. This shows that the kinematical constraints have separated out events with recoil nuclei other than ^4He from the coherent data sample. Additional confirmation of the separation of the coherent from the incoherent events was obtained by comparing the t-distributions of the two samples.

A fit of an exponential form A e^{bt} to the t-distribution of the incoherent event sample yielded a slope parameter b = 9.3 ± 2.0 $(GeV/c)^{-2}$, typical of the nucleon-nucleon slope and expected for incoherent production. A fit to the coherent event sample, on the other hand, gave an exponential slope of b = 42 ± 2 $(GeV/c)^{-2}$, which is close to the slope of the ^{4}He form factor squared, as expected for coherent scattering.

Of the events in the coherent sample, 75% fitted the $p^4He \to {}^4He\, p\pi^+\pi^-$ hypothesis. For a third of these events, the π^+ and the p assignments to the particles with positive sign could be exchanged, without significantly affecting the value of the χ^2 probability. Using the information from the Čerenkov counters this fraction was reduced by a factor of three. For the remaining events, the assignment ambiguity was resolved by using the method of Gajewski et al. [8], which is based on the fit probability and the abundance of the events in the data.

Corrections for the acceptance of the apparatus were made using a Monte Carlo routine to assign weights to the events. Each measured event was rotated around the beam axis by a random angle, and the position of the vertex was chosen at random within the target. For each combination of azimuthal angle and vertex position, a check was made whether such an event would have been detected by the apparatus or not. If, after 100 attempts, the number of accepted events was less than 10, another 100 tries were made, up to a maximum of 1000. The acceptance weight was then taken as the number of generated events divided by the number of accepted events. The most probable acceptance weight for $p\pi^+\pi^-$ events was approximately 3. Events with an acceptance weight greater than 30 were disregarded in the final analysis. The correction for events that had not been accepted at all by the apparatus was estimated using a second Monte Carlo program. Three-prong events were generated simulating N^* production and decay, assuming isotropic decay angular distribution in the centre of mass of the produced system. These events were then passed through the acceptance weighting program. Zero-acceptance events were taken to be those for which the weight obtained was greater than 30. The fraction of such events as a function of the various effective masses and angular variables

used in the data analysis were then used to correct the observed event distributions in these variables. The corrections for zero-acceptance events were approximately 10% at a mass of 1.8 GeV/c^2 and around 45% at 2.8 GeV/c^2. The corrections were also calculated assuming various types of non-isotropic decay angular distributions. The variations in the corrections going from one assumption about the angular distribution to another were found to be smaller than the statistical errors of the data.

Further details of the data analysis are given elsewhere [9].

4. RESULTS

A total of 2576 3C and 4C $p\pi^+\pi^-$ events were obtained. Of these, 996 were detected with the 27 μm target and 1580 with the 8 μm target. The t-ranges covered in the two cases where $0.07 \leq |t| \leq 0.14$ $(GeV/c)^2$ and $0.05 \leq |t| \leq 0.15$ $(GeV/c)^2$, respectively.

4.1 Mass distribution

The mass distribution for all weighted $p\pi^+\pi^-$ events with $0.07 \leq |t| \leq 0.14$ is shown in Fig. 3. The shaded part of the histogram shows those events which have a $p\pi^+$ effective mass within the $\Delta^{++}(1232)$ mass region, $1.1 < M(p\pi^+) < 1.35$ GeV/c^2. Both distributions exhibit the two enhancements at 1.5 GeV/c^2 and 1.7 GeV/c^2 found in other experiments using proton or nuclear targets and incident protons. These enhancements are probably associated with the resonance states seen in formation experiments at lower incident energies. However, as the lower enhancement is close to cut-off, it could possibly also be due to the Deck mechanism, in which it is assumed that the incident proton dissociates into Δ^{++} and π^-, with the π^- being scattered from the target ^{4}He.

The shaded mass distributions of Fig. 3 have therefore been fitted to expressions based on the following hypotheses:

a) A Deck mass enhancement of a form suggested by Stodolsky [10]:

$$W_1 \times \frac{e^{bt_{min}}}{t_{min}} \times \text{(phase space for } p^4He \rightarrow \Delta^{++}\pi^{-4}He) \text{ ,}$$

where

$t_{min} = \left[(m_f^2 - m_i^2)/2p_i\right]^2$,

m_i = mass of the incident proton,

m_f = mass of the produced $p\pi^+\pi^-$ system,

p_i = momentum of the incident proton,

b = exponential slope parameter of the distribution in four-momentum transfer squared,

plus two Breit-Wigner resonances with masses M_1 and M_2, and widths Γ_1 and Γ_2:

$$\frac{W_2}{(M_1-m_f)^2 + (\Gamma_1/2)^2} + \frac{W_3}{(M_2-m_f)^2 + (\Gamma_2/2)^2} \cdot$$

W_1, W_2, and W_3 are the relative weights of the different contributions.

b) Phase space for $p^4He \rightarrow p\pi^+\pi^-{}^4He$, *plus* two Breit-Wigner resonances.

c) A Deck mass enhancement, *plus* one Breit-Wigner resonance.

The relative weights W_n, the masses M_n, and the widths Γ_n, were treated as free parameters. The results are shown in Table 1. The fits to the hypotheses with two Breit-Wigner resonances (a and b) give good results, whereas the fit to the hypothesis with only one Breit-Wigner resonance (c) is poor. This suggests that at least some contribution from a resonance in the 1.5 GeV/c^2 region is required.

The distribution in effective mass of the $p\pi^+$ sub-system is shown in Fig. 4 for six $p\pi^+\pi^-$ mass bins. Three-body phase space has been superimposed, normalized to the total number of events (weighted) in each plot. As is seen, a considerable fraction of the produced $p\pi^+\pi^-$ states with a mass below 2 GeV/c^2 contains the quasi-two-body state $\Delta^{++}\pi^-$.

Similar plots for the $p\pi^-$ system in Fig. 5 show an enhancement above phase space for $p\pi^+\pi^-$ masses between 1.45 GeV/c^2 and 1.95 GeV/c^2. However, in this

case the position of the enhancement varies from a value of approximately 1.2 GeV/c^2 in Fig. 5b to 1.5 GeV/c^2 in Fig. 5e, which can be explained by assuming the enhancement to be a kinematical reflection of the Δ^{++} peak. In the quasi-two-body decay $N^* \to \Delta^{++}\pi^-$, $\Delta^{++} \to p\pi^+$ the effective mass of the $p\pi^-$ sub-system may be expressed as a function of the N^* mass and the decay angle of the proton in the Δ^{++} frame ($\cos\theta'$). A graph of the $p\pi^-$ mass versus the N^* mass for forward ($\cos\theta' = 1$) and backward ($\cos\theta' = -1$) decays of the Δ^{++} is shown in Fig. 6. Plotted on the same graph are the positions of the $p\pi^-$ enhancements, estimated from Fig. 5, which are seen to agree well with the calculation.

The distributions of the $\pi^+\pi^-$ effective mass are shown in Fig. 7. They exhibit no significant enhancements. No reflection of the Δ^{++} is expected to appear in the $\pi^+\pi^-$ distribution, as can be seen from the graph of the reflected $\pi^+\pi^-$ mass in Fig. 8. The large differences between the forward and backwards decays of the proton spreads the reflection across most of the available phase space.

The relative content of $\Delta^{++}\pi^-$ in the $p\pi^+\pi^-$ system for different $p\pi^+\pi^-$ masses may be estimated from the $p\pi^+$ mass distributions in Fig. 4. Each distribution has been fitted to three-body phase space for the $p\pi^+\pi^-$ final state at the mean $p\pi^+\pi^-$ mass for each plot, superimposing a Breit-Wigner function with parameters M = = 1.23 GeV/c^2, Γ = 0.12 GeV/c^2. The relative contributions were used to calculate the branching ratio, given in Table 2. No results are given for masses below 1.55 GeV/c^2, since for these events the $p\pi^+$ mass is in any case constrained to be essentially within the $\Delta^{++}(1232)$ mass region for purely kinematical reasons.

4.2 Distribution in t

The t-distribution of the $p\pi^+\pi^-$ events is shown in Fig. 9. A fit to the exponential form $A\, e^{bt}$ in the range $0.065 \leq |t| \leq 0.135$ (GeV/c)^2 yields a slope parameter $b = 42 \pm 2$ (GeV/c)$^{-2}$. The fitted slope parameter as a function of mass is plotted in Fig. 10. The slope is seen to have a tendency to decrease with increasing $p\pi^+\pi^-$ mass. This behaviour is similar to that observed in experiments on $p\pi^+\pi^-$ production from hydrogen, where the slope has been found to decrease from

around 15 $(GeV/c)^{-2}$ at a $p\pi^+\pi^-$ mass of 1.4 GeV/c to around 5 $(GeV/c)^{-2}$ at a mass of 1.8 GeV/c [11]. The results are approximately consistent with the impulse approximation (except for the point at 1.4 GeV/c^2) which predicts that the slopes of the elementary amplitude and of the ^{4}He form factor are additive. The line in Fig. 10 indicates this prediction using a slope of the ^{4}He form factor squared of 32 $(GeV/c)^{-2}$.

4.3 Distributions of decay polar angles

The distributions of the polar angle of the $p\pi^+\pi^-$ decay plane normal in the t-channel helicity frame, cos β_t, are shown in six $p\pi^+\pi^-$ mass bins in Fig. 11. The lack of isotropy of these distributions suggests that the associated $p\pi^+\pi^-$ states have spins greater than $\frac{1}{2}$. The asymmetry of a distribution, such as that of Fig. 11e, indicates the interference between several partial waves of different parity in the corresponding mass region.

The distributions of the polar angle of the Δ^{++} direction of motion in the t-channel helicity frame cos θ_t are shown in Fig. 12. Only those events for which the $p\pi^+$ mass lies within the $\Delta^{++}(1232)$ mass band, 1.1-1.3 GeV/c^2, have been included. The non-uniform shape of these distributions again shows the presence of a $p\pi^+\pi^-$ state with spin greater than $\frac{1}{2}$, and the slight asymmetry below a $p\pi^+\pi^-$ mass of 1.65 GeV/c^2 (Figs. 12a, b, and c) suggests interference between partial waves in this mass region. Within statistical errors, the distributions are symmetric above 1.65 GeV/c^2.

4.4 Moments analysis

The decay angular distributions have been decomposed in terms of spherical harmonic moments by evaluation of the integrals

$$\langle Y_\ell^0(z)\rangle = \int_{-1}^{1} Y_\ell^{m=0}(z)\cdot W(z)\, dz\,, \qquad \ell = 1,\ 6,$$

where $Y_\ell^{m=0}(z)$ is the ℓ^{th} spherical harmonic function with m = 0, and W(z) is the observed distribution of either $z = \cos\beta_t$ or $z = \cos\theta_t$. The moments have been evaluated in 12 $p\pi^+\pi^-$ mass bins for each of the 6 ℓ-values separately; the results are shown in Figs. 13 and 14.

In these plots the $\ell = 2$ moment is significantly different from zero, over the whole $p\pi^+\pi^-$ mass range for the case of cos β_t, and in the mass range above 1.65 GeV/c^2 for the case of cos θ_t. The $\ell = 1$ moment for cos θ_t seems to deviate from zero in the region below 1.55 GeV/c^2. Other moments also show signals, but their significance is not strong, and in most cases their values are consistent with zero throughout the whole mass range.

The conclusions that can be drawn from this analysis are:

i) In the region 1.4-1.6 GeV/c^2 the signal noted in the odd $\langle Y_1^0(\cos\theta_t)\rangle$ moment (this signal is in agreement with the slight asymmetry observed for the cos θ_t distribution in Section 4.3) suggests the presence of several interfering partial waves in this mass region.

ii) In the region 1.65-1.75 GeV/c^2 the $\langle Y_2^0(z)\rangle$ moment shows significant signals for both $z = \cos\beta_t$ and $z = \cos\theta_t$, whereas the other moments are close to zero. This is consistent with the presence of a single angular momentum state of spin $J \geq 3/2$ in this mass region.

4.5 Spin assignment

The moments analysis suggests that the mass region between 1.65 GeV/c^2 and 1.75 GeV/c^2 is dominated by a single spin state with $J \geq 3/2$. We have therefore fitted the folded angular distributions in the two $p\pi^+\pi^-$ mass bins, 1.65 GeV/c^2 to 1.70 GeV/c^2 and 1.70 to 1.75 GeV/c^2, with expressions which can be formulated assuming the presence of a single state of spin. These expressions are explicitly given in the paper by Rhode et al. [12], where the cos β and cos θ distributions are expressed in terms of the ratios $G = R_{3/2+}/R_{1/2+}$ and $G' = R_{5/2+}/R_{1/2+}$ of phenomenological decay parameters and the N^* and Δ^{++} spin-density matrix elements ρ_{11} and ρ'_{11} for the cases of spin 3/2 and spin 5/2.

The folded cos β_t distributions were fitted to the spin 3/2 and spin 5/2 hypotheses. The over-all normalization and ρ_{11}, G, and G′ were treated as free parameters in the fit with the restriction $0 \leq \rho_{11} \leq 0.5$. From the results, given in Table 3, neither of the spin hypotheses can be given a preference over the other.

The results of a fit to the folded cos θ_t distributions are given in Table 4. The ratio $R = \rho'_{11}/(\frac{1}{2} - \rho'_{11})$ and ρ_{11} were free parameters in the fit with $0 \leq \rho_{11} \leq 0.5$. Theoretical values of the parameter R are given in Table 5, and a comparison with the measured values shows that the more probably parity assignment is negative for spin $\frac{3}{2}$ and positive for spin $\frac{5}{2}$. In the lower mass bin the spin $\frac{5}{2}$ assignment has a somewhat higher fit probability than the spin $\frac{3}{2}$ assignment. Another indication in favour of the spin $\frac{5}{2}$ assignment is that the decay of a $\frac{3}{2}^-$ state to $\Delta^{++}\pi^-$ would result in a uniform cos θ_t distribution, contrary to that observed in Fig. 12d.

Joint fits have also been made to cos θ_t and cos θ', where θ' is the polar angle of the proton in the Δ^{++} rest system, minimizing the sum of the two χ^2; ρ_{11} and $\langle\rho'_{11}\rangle$ were free parameters in the fit, and the value of R was calculated from these two quantities. The results, given in Table 6, again show some preference based on the fit probability for spin $\frac{5}{2}$ in the lower mass bin. For the higher mass bin the R values give some preference to the $\frac{5}{2}^-$ assignment.

As a result of these fits, there is some indication that the spin of the $p\pi^+\pi^-$ state around 1.7 GeV/c^2 is $\frac{5}{2}$.

4.6 Azimuthal angles; s- and t-channel helicity conservation

Conservation of helicity in the s-channel was originally proposed as a general property of diffractive processes. On the other hand, experiments on diffractive production of $p\pi^+\pi^-$ systems from hydrogen have found consistency with t-channel rather than s-channel helicity conservation [13].

A necessary but not sufficient condition for helicity conservation in either channel, with an unpolarized beam, is that the decay products should have a uniform azimuthal distribution in the corresponding reference frame.

The azimuthal angle of the decay plane normal, ϕ, and that of the Δ^{++} direction, ψ, are shown for the six mass bins in Figs. 15-18. Given the limited statistics, it is not possible to make firm conclusions about the isotropy or anisotropy

of these distributions. Comparing, however, the s-channel distributions (ϕ_s in Fig. 15 and ψ_s in Fig. 16) with the t-channel distributions (ϕ_t in Fig. 17 and ψ_t in Fig. 18), the former appear on the average to be somewhat more anisotropic than the latter. This indicates that if helicity is conserved in either the s- or the t-channel, then it is more probably in the t-channel.

5. CONCLUSIONS

The conclusions of the analysis may be summarized as follows.

1. Two enhancements are seen in the coherently produced $p\pi^+\pi^-$ mass distribution, one at 1.49 ± 0.02 GeV/c^2 and the other at 1.71 ± 0.02 GeV/c^2, both with a width around 0.2 GeV/c^2. These enhancements can be well fitted by Breit-Wigner resonances. The lower peak does not seem to be dominantly a Deck-type enhancement.

2. The only quasi-two-body state that is visible in the sub-mass distributions is the $\Delta^{++}\pi^-$ state. The branching ratio of this state is 42 ± 8% in the region of the 1.71 enhancement.

3. The exponential t-slope parameter of the coherent $p\pi^+\pi^-$ production cross-section shows a decrease from around 70 $(\text{GeV/c})^{-2}$ at a $p\pi^+\pi^-$ mass of 1.4 GeV/c^2 to around 35 $(\text{GeV/c})^{-2}$ at a $p\pi^+\pi^-$ mass of 2 GeV/c^2.

4. In the $p\pi^+\pi^-$ mass region 1.4-1.6 GeV/c^2 the $\langle Y_1^0(\cos\theta)\rangle$ angular moment is different from zero, indicating the presence of several interfering partial waves. In the 1.65-1.75 GeV/c^2 region only the $\langle Y_2^0(\cos\beta)\rangle$ and $\langle Y_2^0(\cos\theta)\rangle$ moments show significant signals, consistent with the presence of a single state with spin > $^3/_2$.

5. Fits to the angular distribution in the 1.65-1.75 GeV/c^2 mass region, subject to the assumption that a single state is dominant, indicate some preference for a spin assignment of $^5/_2$.

6. A study of the azimuthal decay angles indicates that, if helicity is expected to be conserved in either the s- or the t-channel, then it is more probably in the latter.

For the reasons discussed in the Introduction, it is of interest to compare these results with those obtained in proton-target experiments on $p\pi^+\pi^-$ production at similar energies [11-15]. Except for the t-distribution, in which case the impulse approximation may be used for comparison with the proton-target data, our distributions have been directly compared with those of the proton-target experiments. Such a comparison reveals a remarkable similarity.

This similarity is most apparent in the details of the mass distributions and of the angular moments. The position and width of the mass enhancement at 1.71 GeV/c^2 agree within errors with the results of both Rhode et al. [12] and Rushbrooke et al. [14]. The position of the mass enhancement at 1.49 GeV/c^2 is about 0.5 GeV/c^2 higher in energy and its width is about twice as large as those of the enhancements discussed in Refs. 12 and 14. However, the difference is only on the level of one or two standard deviations. The branching ratio of 42 ± 8% for the $\Delta^{++}\pi^-$ state in the 1.7 GeV/c^2 region agrees with the values of 35 ± 20% found by Rushbrooke et al. [14] and 40 ± 10% by Blobel et al. [15].

The evaluation of the slopes of the nucleon target production amplitudes cannot be done with good accuracy from our data, owing to the large errors. Double scattering in the ^{4}He nucleus, which should be taken into account in a more accurate evaluation, also entails some uncertainties. However, using the impulse approximation there is agreement with the slope values found by Johnstad et al. [11], except in the lowest mass bin where our slope of 70 ± 7 $(\text{GeV/c})^{-2}$ is higher than the value of approximately 50 $(\text{GeV/c})^{-2}$ that would be expected from the data of the same reference.

Results from moments analysis of the decay angular distributions in proton-target experiments are reported by Johnstad et al. [11], Rhode et al. [12], and Rushbrooke et al. [14]. Comparing the results in these references, obtained with the $p\pi^+\pi^-$ decay plane normal as analyser, with our results in Fig. 13 reveals a remarkable agreement. The conclusion from Fig. 13 that the $\ell = 2$ moment is different from zero at all masses and that the other moments, up to $\ell = 6$, are consistent with zero, is generally true for all three analyses.

When the Δ^{++} direction of motion is used as analyser, the comparatively rapid rise of the $\ell = 2$ moment above a mass of 1.60 GeV/c^2, shown in Fig. 14, is also present in the data of Johnstad et al. [11] and of Rushbrooke et al. [14]. The significant positive signal for the $\ell = 1$ moment at lower masses, indicating interfering partial waves, is also found in both these analyses. At masses above 1.8 GeV/c^2 the proton-target data show deviations from zero for nearly all ℓ-values between 1 and 6. This is not reproduced by our data, which however, is hardly a significant difference, as the error bars are very large in this region.

The indication that the 1.71 GeV/c^2 enhancement in the proton-target data is dominantly a spin $^5/_2$ state, which has been found by Johnstad et al. [11] and by Rhode et al. [12], agrees with our data, and the preference for t-channel rather than s-channel helicity conservation found in the proton-target experiments of Rushbrooke et al. [14] and of Blobel et al. [15] is also in accordance with our results.

The similarity between the data describing the coherent production of $p\pi^+\pi^-$ on a ^{4}He target and the production of $p\pi^+\pi^-$ on a proton target suggests that the dominance of isospin zero exchange, which is imposed by the nuclear coherence condition in the He target case, is also present in the case of a proton target. There are secondary Regge trajectories that have isospin zero and which for this reason would be allowed exchanges in the case of coherent production. However, we see no reason why the exchange of these trajectories would be much bigger than the exchange of isospin-one trajectories, which seem to be small in the case of a proton target. We therefore conclude that our data give some independent support to the idea that vacuum exchange, i.e. diffraction dissociation, dominates in the production of low-mass $p\pi^+\pi^-$ states at incident momenta around 20 GeV/c.

This experiment was carried out at CERN using the 28 GeV Proton Synchrotron, with financial support from CERN, the Swedish Atomic Research Council, and the Science Research Council of the United Kingdom. We would like to thank the CERN-Munich group for having put their spectrometer at our disposal. It is a great pleasure to thank our colleagues C. Curran, P. Grafström and A.L. Read for their contributions to the experiment. We would also like to express our gratitude to R. Lorenzi and H. Watson for their invaluable technical assistance throughout the course of the experiment.

REFERENCES

[1] S. Dahlgren et al., Nuclear Instrum. Methods 89 (1970) 29.

[2] J.K. Davies et al., Nuclear Instrum. Methods 129 (1975) 313.

[3] U. Brotschi et al., Nuclear Instrum. Methods 129 (1975) 39.

[4] G. Charpak et al., Nuclear Instrum. Methods 24 (1963) 501.

[5] K. Gustafsson et al., Nuclear Instrum. Methods 117 (1974) 171.

[6] G. Grayer et al., Nuclear Phys. B75 (1974) 189.

[7] T. Ekelöf et al., Proton-^{4}He elastic scattering and coherent single-pion production at 18.6 GeV/c, submitted to Nuclear Phys. B (1977).

[8] W. Gajewski et al., Université libre de Bruxelles, Bulletin 38 (1968).

[9] P.C. Bruton, University of London, Ph.D. Thesis (1977).
S.M. Fisher, University of London, Ph.D. Thesis (1977).

[10] L. Stodolsky, Phys. Rev. Letters 18 (1967) 973.

[11] H. Johnstad et al., Nuclear Phys. B42 (1972) 558.

[12] J.I. Rhode et al., Phys. Rev. 187 (1969) 1844.

[13] J.G. Rushbrooke et al., Nuclear Phys. B35 (1971) 1.

[14] J.G. Rushbrooke et al., Phys. Rev. D4 (1971) 3273.

[15] V. Blobel et al., Nuclear Phys. B97 (1975) 201.

Table 1

Summary of results from the χ^2 fits to the $p\pi^+\pi^-$ mass distribution in which the $p\pi^+$ mass has been restricted to values 1.10–1.35 GeV/c^2 (the shaded distribution in Fig. 3) .

Hypothesis	χ^2	ν	Prob. (%)	Relative weights			M_1 (GeV/c^2)	Γ_1 (GeV/c^2)	M_2 (GeV/c^2)	Γ_2 (GeV/c^2)
				Deck W_1	Breit-Wigner (1500) W_2	Breit-Wigner (1700) W_3				
(a)	15.4	16	49	0.23	0.39	0.38	1.49 ± 0.025	0.221 ± 0.011	1.71 ± 0.024	0.208 ± 0.04
(b)	17.1	17	45	-	0.51	0.49	1.49 ± 0.009	0.201 ± 0.007	1.72 ± 0.014	0.200 ± 0.022
(c)	33.5	19	2	0.70	-	0.30	-	-	1.66 ± 0.018	0.233 ± 0.011

Table 2

Summary of results from the calculations of the $N^* \to \Delta^{++}\pi^-$ branching ratio (from the mass distributions in Fig. 4).

Mass bin (GeV/c^2)	Branching ratio $r = \frac{N^* \to \Delta^{++}\pi^-}{N^* \to p\pi^+\pi^- \text{ (all modes)}}$
$1.55 < M < 1.65$	0.78 ± 0.16
$1.65 < M < 1.75$	0.42 ± 0.08
$1.75 < M < 1.95$	0.50 ± 0.21
$1.95 < M < 2.15$	0.26 ± 0.16

Table 3

Summary of results from the χ^2 fits to the cosine of the polar angle of the decay plane normal $\cos \beta_t$ (the distributions shown in Fig. 11 folded around $\cos \beta_t = 0$).

Mass	J	ρ_{11}	G	G′	χ^2 prob. (%)
$1.65 < M_{p\pi\pi} < 1.7$	$\frac{3}{2}$	0.32 ± 0.05	10.6 ± 0.9	-	34
	$\frac{5}{2}$	-	2.3 ± 1.8	2.2 ± 1.2	42
$1.7 < M_{p\pi\pi} < 1.75$	$\frac{3}{2}$	0.31 ± 0.05	10.9 ± 0.9	-	69
	$\frac{5}{2}$	-	1.4 ± 1.0	1.6 ± 0.7	70

Table 4

Summary of results from the χ^2 fits to the cosine of the polar angle of the Δ^{++} direction of motion cos θ_t (the distributions shown in Fig. 12 folded around cos θ_t = 0).

Mass	J	ρ_{11}	R	χ^2 prob. (%)
1.65 < M < 1.7	$\frac{3}{2}$	$0.40 \begin{smallmatrix} + 0.10 \\ - 0.30 \end{smallmatrix}$	1.04 ± 0.43	27
	$\frac{5}{2}$	$0.5 \begin{smallmatrix} + 0.0 \\ - 0.04 \end{smallmatrix}$	1.15 ± 0.73	61
1.7 < M < 1.75	$\frac{3}{2}$	$0.49 \begin{smallmatrix} + 0.01 \\ - 0.10 \end{smallmatrix}$	1.29 ± 0.34	15
	$\frac{5}{2}$	$0.5 \begin{smallmatrix} + 0.0 \\ - 0.01 \end{smallmatrix}$	1.27 ± 0.61	15

Table 5

Theoretically calculated R values for different values of J^P and ℓ

J^P \ ℓ	0	1	2	3	4
$3/2^-$	1		1		
$3/2^+$		1/9		9	
$5/2^-$			1/6		6
$5/2^+$		3/2		2/3	

Table 6

Summary of results from the joint χ^2 fit to cos θ_t and cos θ', the cosines of the polar angles of the directions of the Δ^{++} and the proton, respectively (the distributions are folded around cos θ_t = 0 and cos θ' = 0, respectively).

Mass	J	ρ_{11}	$\langle\rho'_{11}\rangle$	R	χ^2 prob.
1.65 < M < 1.7	$\frac{3}{2}$	$0.48\ ^{+\ 0.02}_{-\ 0.44}$	0.35 ± 0.015	2.37 ± 0.34	44%
	$\frac{5}{2}$	$0.39\ ^{+\ 0.11}_{-\ 0.17}$	0.37 ± 0.018	2.88 ± 0.55	67%
1.7 < M < 1.75	$\frac{3}{2}$	$0.50\ ^{+\ 0.0}_{-\ 0.10}$	0.40 ± 0.046	3.83 ± 2.14	44%
	$\frac{5}{2}$	0.27 ± 0.13	0.42 ± 0.048	5.7 ± 4.4	35%

Figure captions

Fig. 1 : Plan view of the layout of the experimental apparatus. The gaseous helium target is placed on the beam axis inside the helium recoil spectrometer, which contains spark chambers and 7 circumferential scintillators. The forward spectrometer consists of 7 MWPCs and 48 spark chambers in front of and behind the large-aperture spectrometer magnet. The identities of the particles are obtained from the signals of the two modular Čerenkov counters R and T. The other capital letters in the figure indicate trigger scintillators referred to in the text.

Fig. 2 : The distribution for fitted coherent events of the ratio $\chi = (E_{PH} - E_{TOF})/\sqrt{\sigma E_{PH}^2 + \sigma E_{TOF}^2}$, where E_{PH} and E_{TOF} are the recoil energy derived from pulse height and from time of flight, respectively.

Fig. 3 : The $p\pi^+\pi^-$ mass distribution for weighted events with $0.07 \leq |t| \leq 0.14$. The shaded part shows the distribution of events with $p\pi^+$ mass restricted to the interval 1.10-1.35 MeV/c^2.

Fig. 4 : The $p\pi^+$ mass distribution for different intervals of $p\pi^+\pi^-$ mass. The curves are the calculated phase-space distributions, normalized to the total number of weighted events in each plot.

Fig. 5 : The $p\pi^-$ mass distribution for different intervals of $p\pi^+\pi^-$ mass. The curves are as in Fig. 4.

Fig. 6 : The two lines show calculated correlations between the $p\pi^-$ and the $p\pi^+\pi^-$ masses in a quasi-two-body decay $N^* \to \Delta^{++}\pi^-$, $\Delta^{++} \to p\pi^+$ for the cases of forward ($\cos\theta' = 1$) and backward ($\cos\theta' = -1$) decays of the Δ^{++}. The crosses are the positions of the enhancements in the $p\pi^-$ plots of Fig. 5.

Fig. 7 : The $\pi^+\pi^-$ mass distribution for different intervals of the $p\pi^+\pi^-$ mass. The curves are the calculated phase-space distributions, normalized to the total number of weighted events in each plot.

Fig. 8 : The two lines show calculated correlations between the $\pi^+\pi^-$ and $p\pi^+\pi^-$ masses in a quasi-two-body decay $N^* \to \Delta^{++}\pi^-$, $\Delta^{++} \to p\pi^+$ for the case of forward ($\cos\theta' = 1$) and backward ($\cos\theta' = -1$) decays of the Δ^{++}.

Fig. 9 : The distribution in t. The straight line is a fit of the exponential form $A\, e^{bt}$ with $b = 41.9 \pm 2.3\ (GeV/c)^{-2}$ as the result.

Fig. 10 : The exponential slope parameter b for six separate mass bins. The line indicates the impulse approximation prediction.

Fig. 11 : The distributions of the polar angle of the N^* decay plane normal in the t-channel helicity frame, $\cos\beta_t$, for six separate $p\pi^+\pi^-$ mass intervals. Solid line: data corrected for apparatus acceptance, including regions of zero acceptance. Dashed line: without zero-acceptance corrections.

Fig. 12 : The distribution of the polar angle of the Δ^{++} direction of motion in the t-channel helicity frame, $\cos\theta_t$, for events with $p\pi^+$ mass in the Δ^{++} interval 1.1-1.3 GeV/c^2 and for six separate $p\pi^+\pi^-$ mass intervals.

Fig. 13 : The spherical harmonic moments $\langle Y_\ell^0 \rangle$ of the decay plane normal, $\cos\beta_t$, in 12 $p\pi^+\pi^-$ mass bins for ℓ-values from 1 to 6.

Fig. 14 : The spherical harmonic moments $\langle Y_\ell^0 \rangle$ of the Δ^{++} direction of motion, $\cos\theta_t$, in 12 $p\pi^+\pi^-$ mass bins for ℓ-values from 1 to 6.

Fig. 15 : The azimuthal angle ϕ_s of the decay plane normal in the s-frame for six $p\pi^+\pi^-$ mass bins.

Fig. 16 : The azimuthal angle ψ_s of the Δ^{++} direction of motion in the s-frame for six $p\pi^+\pi^-$ mass bins.

Fig. 17 : The azimuthal angle ϕ_t of the decay plane normal in the t-frame for six $p\pi^+\pi^-$ mass bins.

Fig. 18 : The azimuthal angle ψ_t of the Δ^{++} direction of motion in the t-frame for six $p\pi^+\pi^-$ mass bins.

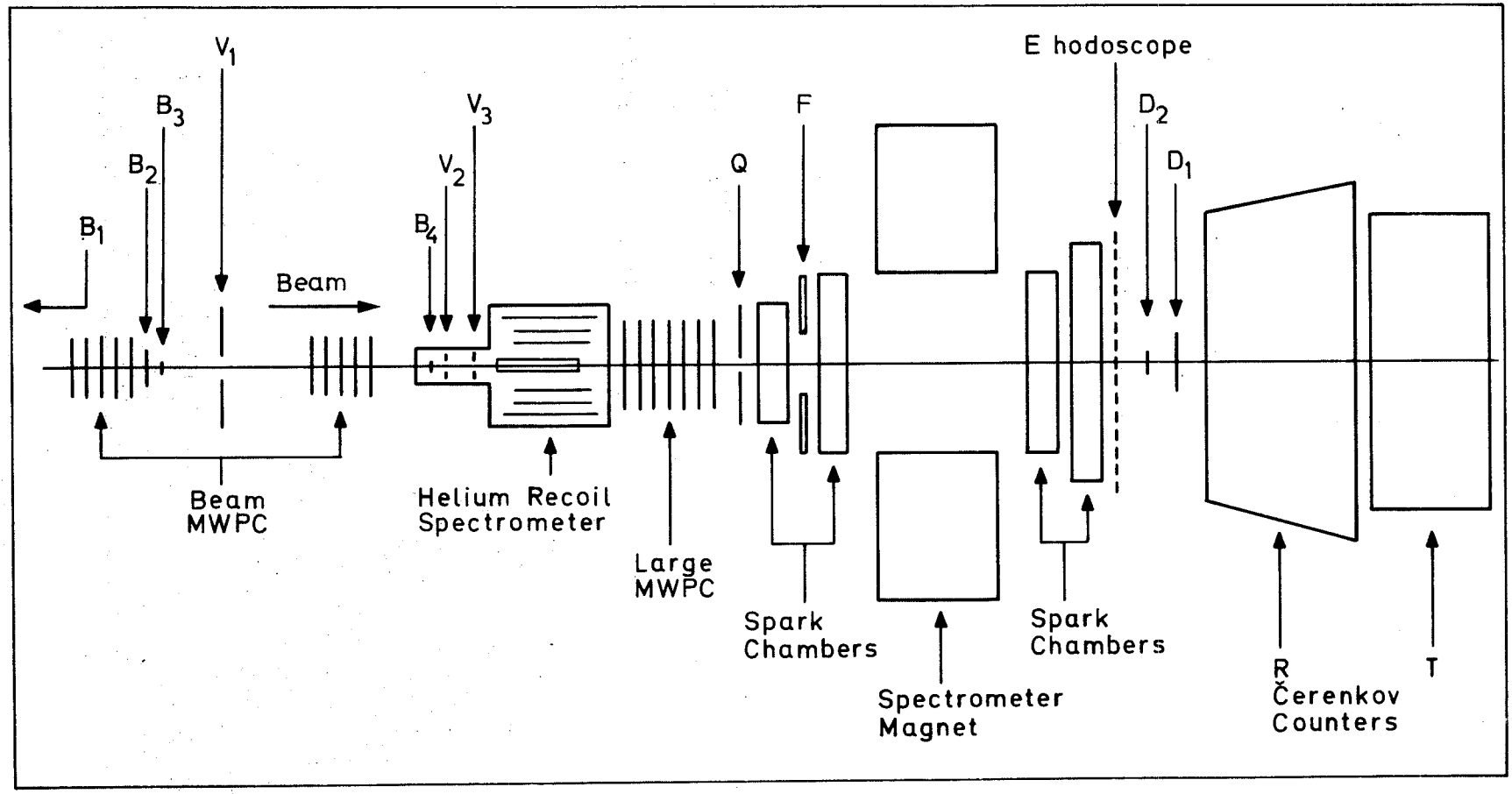
V1
B3
B2
B1
Beam
V3
V2
B4
Q
F
E hodoscope
D2
D1
Beam
MWPC
Helium Recoil
Spectrometer
Large
MWPC
Spark
Chambers
Spectrometer
Magnet
Spark
Chambers
R
Čerenkov
Counters
T

Fig. 1

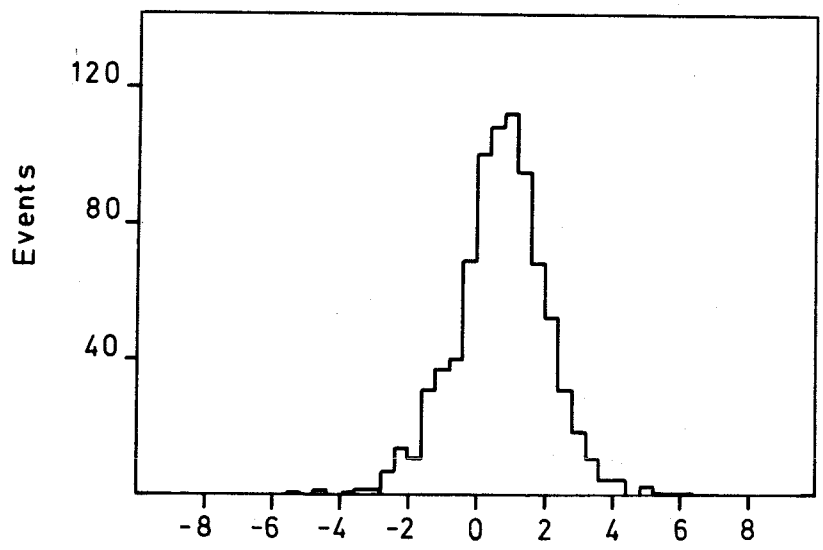
Events
120
80
40
-8
-6
-4
-2
0
2
4
6
8

Fig. 2

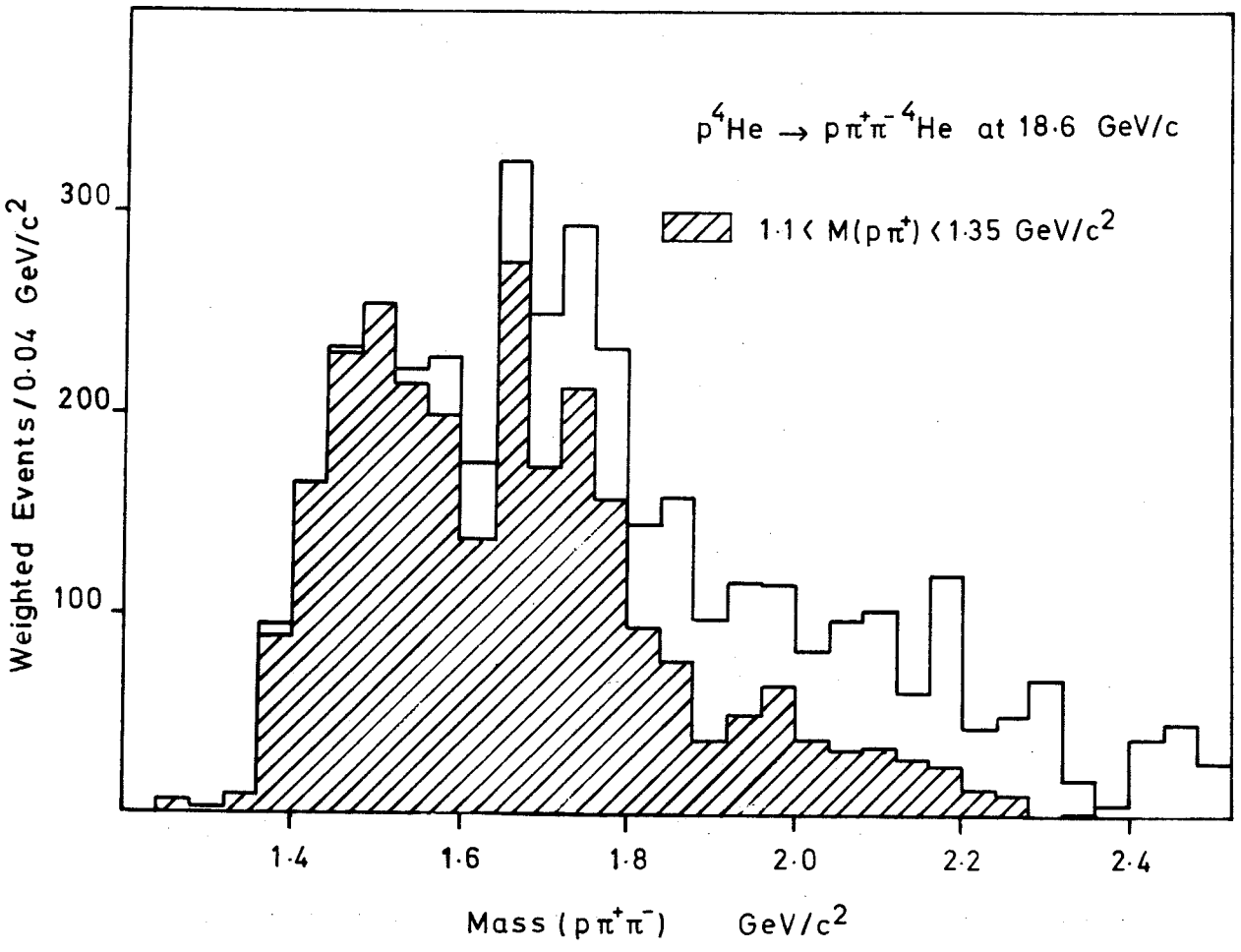
$p^4He \rightarrow p\pi^+\pi^- {}^4He$ at 18·6 GeV/c
1·1 < M(pπ⁺) < 1·35 GeV/c²
Weighted Events / 0·04 GeV/c²
300
200
100
1·4
1·6
1·8
2·0
2·2
2·4
Mass (pπ⁺π⁻) GeV/c²

Fig. 3

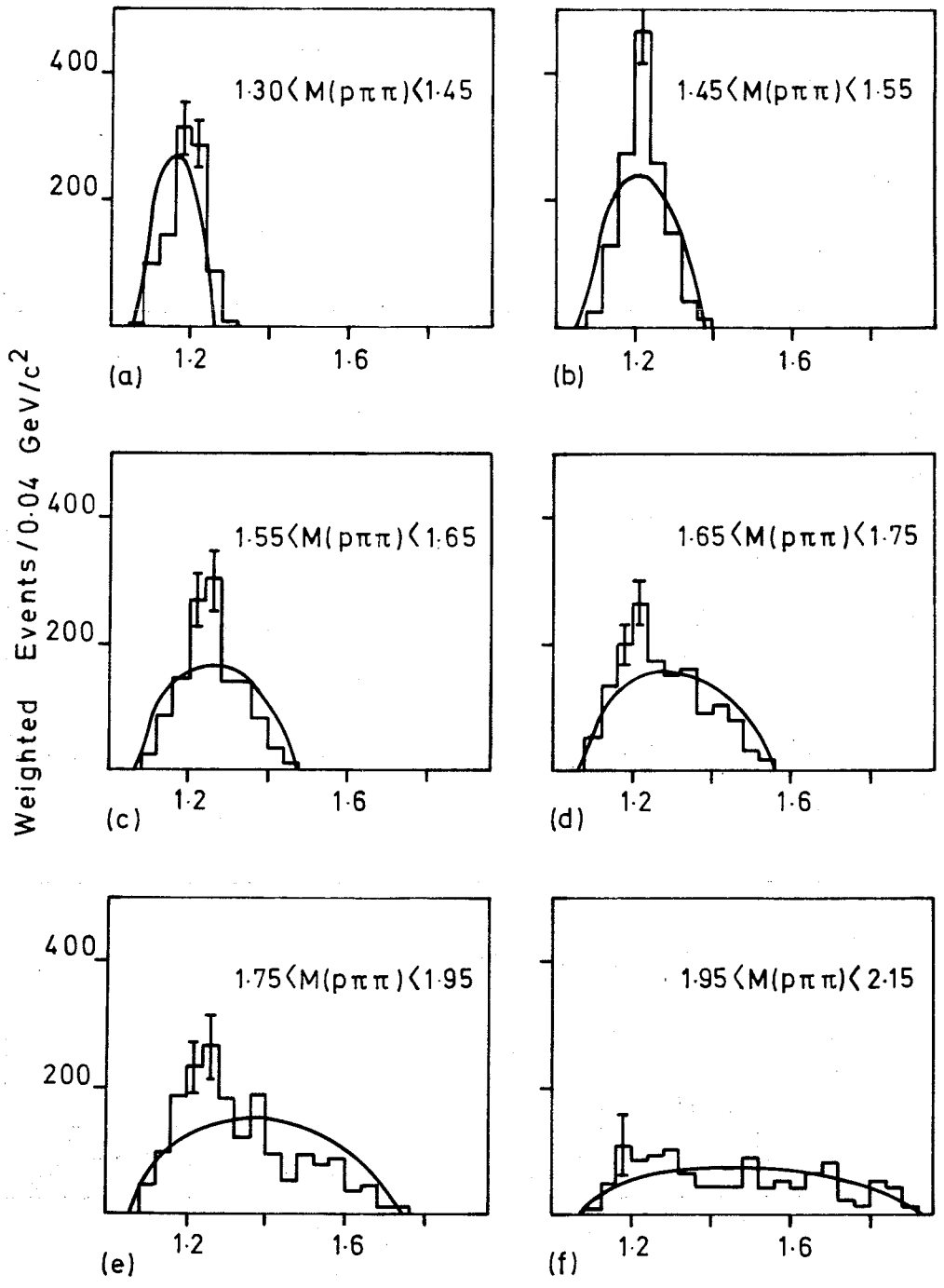
400
200
1·30<M(pππ)<1·45
(a)
1·2
1·6
1·45<M(pππ)<1·55
(b)
1·55<M(pππ)<1·65
(c)
1·65<M(pππ)<1·75
(d)
1·75<M(pππ)<1·95
(e)
1·95<M(pππ)<2·15
(f)
Weighted Events/0·04 GeV/c²
Mass (pπ⁺) GeV/c²

Fig. 4

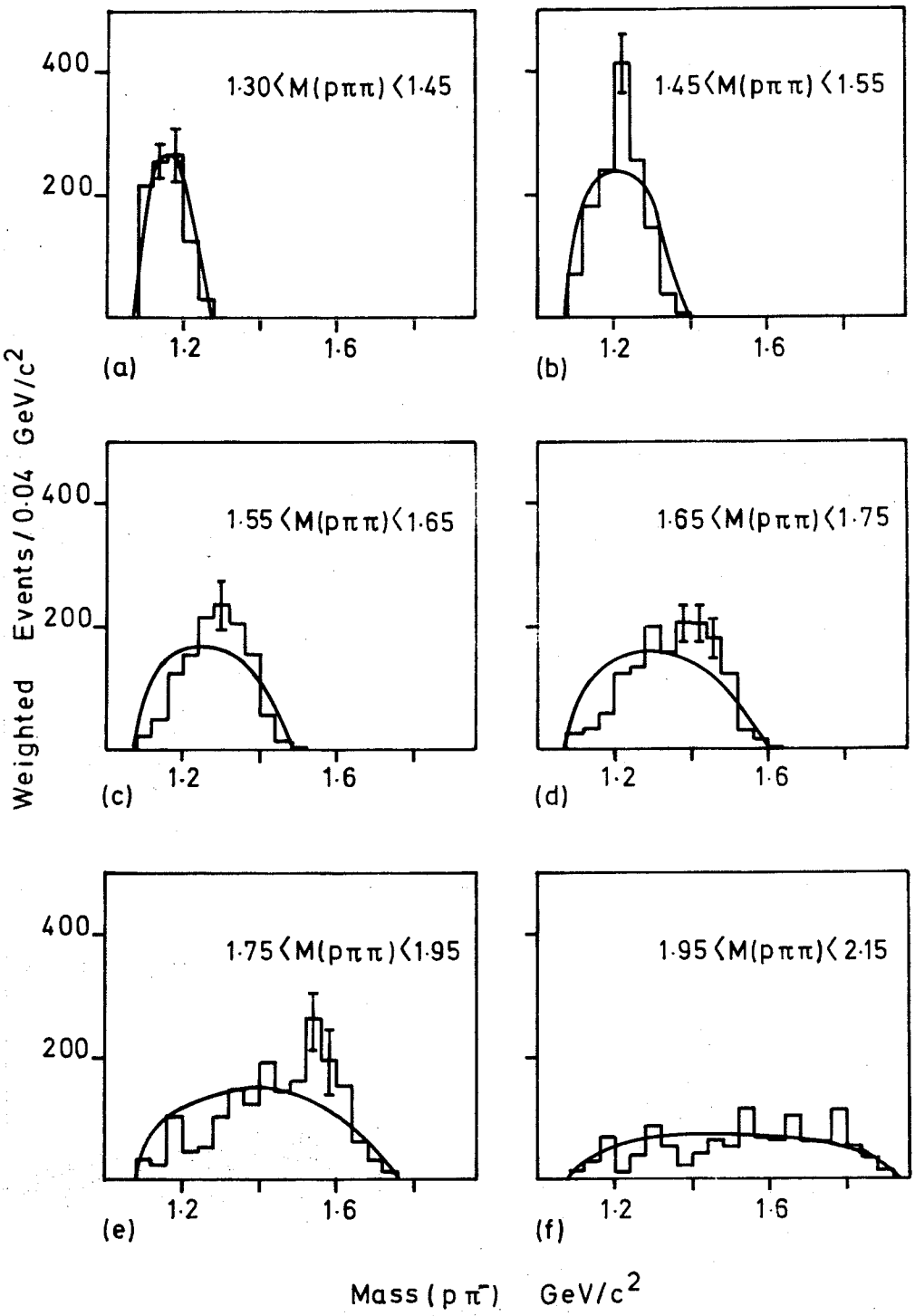
1·30<M(pππ)<1·45
1·45<M(pππ)<1·55
1·55<M(pππ)<1·65
1·65<M(pππ)<1·75
1·75<M(pππ)<1·95
1·95<M(pππ)<2·15
400
200
1·2
1·6
(a)
(b)
(c)
(d)
(e)
(f)
Weighted Events / 0·04 GeV/c²
Mass (pπ⁻) GeV/c²

Fig. 5

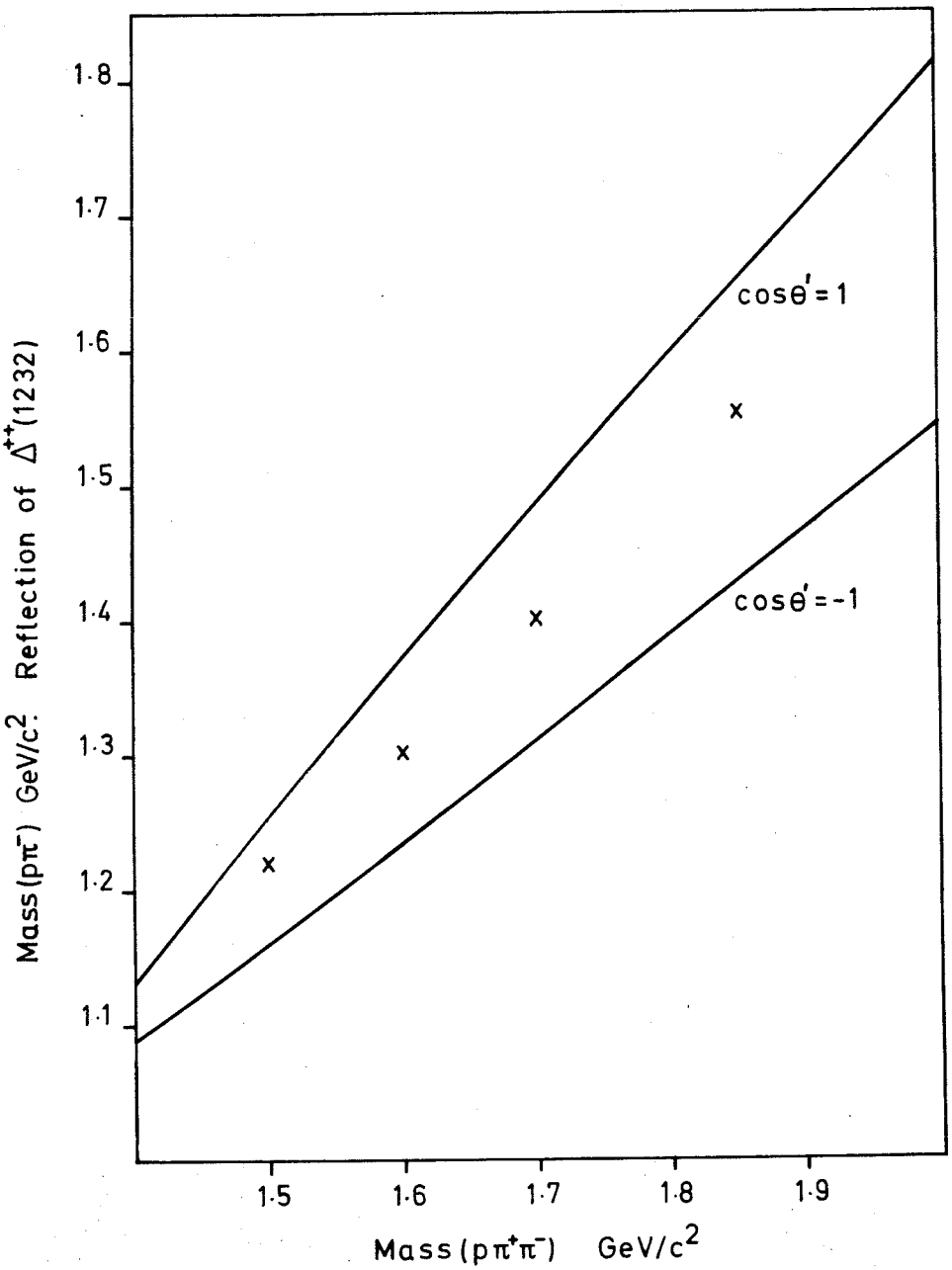
1·8
1·7
1·6
1·5
1·4
1·3
1·2
1·1
Mass(pπ⁻) GeV/c² Reflection of Δ⁺⁺(1232)
cosθ'=1
cosθ'=-1
1·5
1·6
1·7
1·8
1·9
Mass(pπ⁺π⁻) GeV/c²

Fig. 6

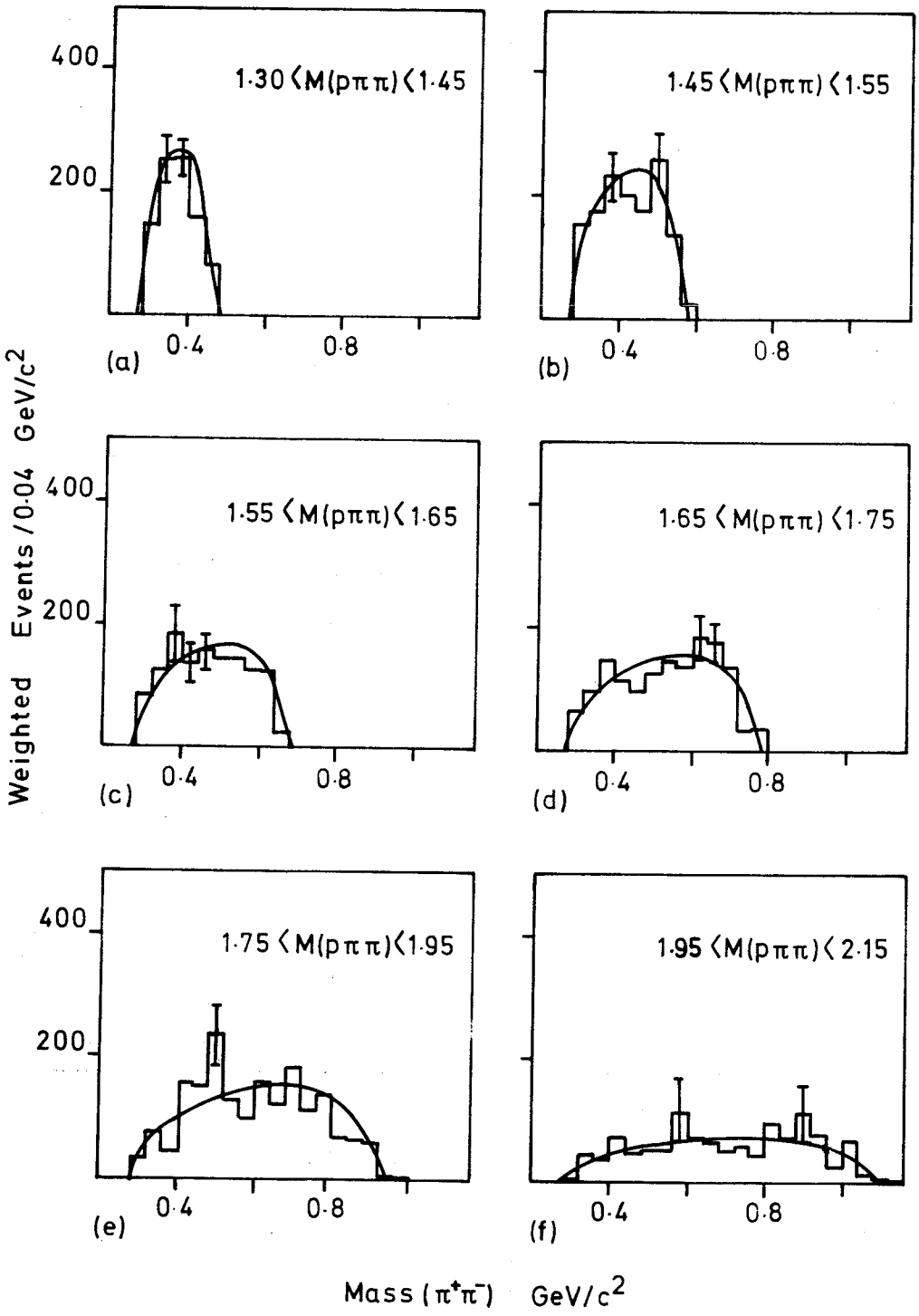
1·30 < M(pππ) < 1·45
1·45 < M(pππ) < 1·55
1·55 < M(pππ) < 1·65
1·65 < M(pππ) < 1·75
1·75 < M(pππ) < 1·95
1·95 < M(pππ) < 2·15
(a)
(b)
(c)
(d)
(e)
(f)
400
200
0·4
0·8
Weighted Events / 0·04 GeV/c²
Mass (π⁺π⁻) GeV/c²

Fig. 7

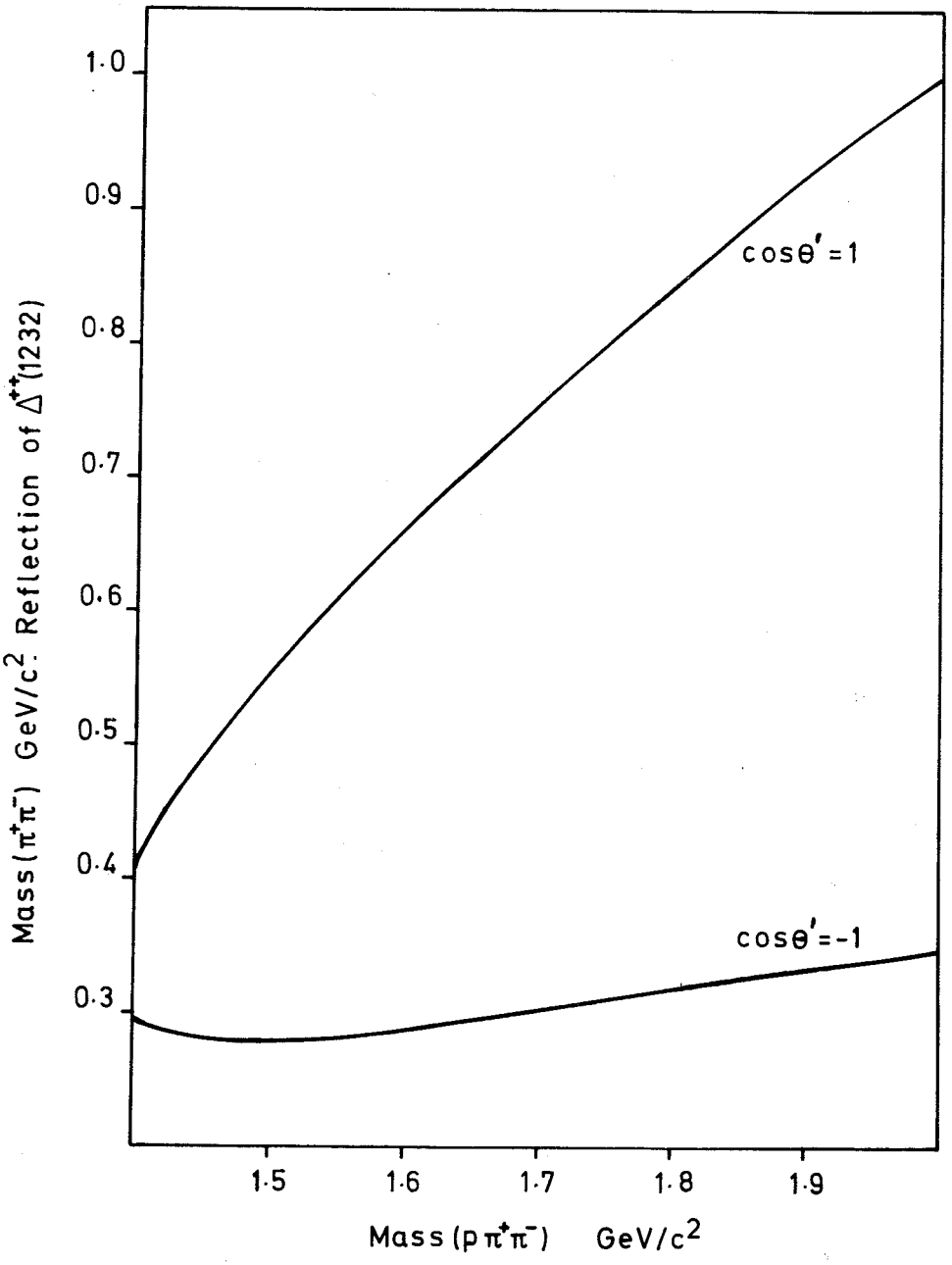
1·0
0·9
0·8
0·7
0·6
0·5
0·4
0·3
Mass $(\pi^+\pi^-)$ GeV/c^2 Reflection of $\Delta^{++}(1232)$
$\cos\theta' = 1$
$\cos\theta' = -1$
1·5
1·6
1·7
1·8
1·9
Mass $(p\pi^+\pi^-)$ GeV/c^2

Fig. 8

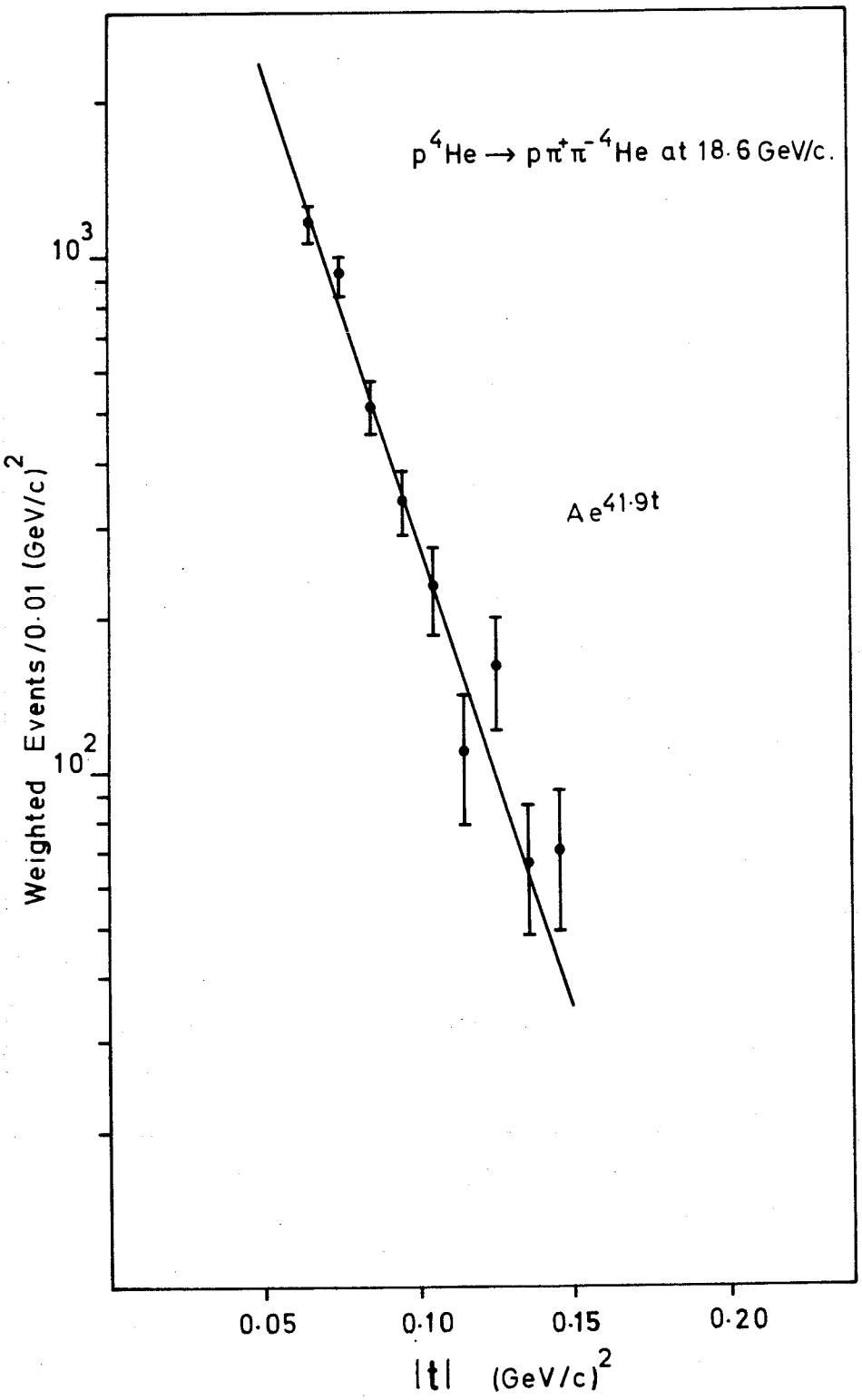
$p^4He \rightarrow p\pi^+\pi^-{}^4He$ at 18.6 GeV/c.
$Ae^{41.9t}$
Weighted Events/0.01 $(GeV/c)^2$
10^3
10^2
0.05
0.10
0.15
0.20
$|t|$ $(GeV/c)^2$

Fig. 9

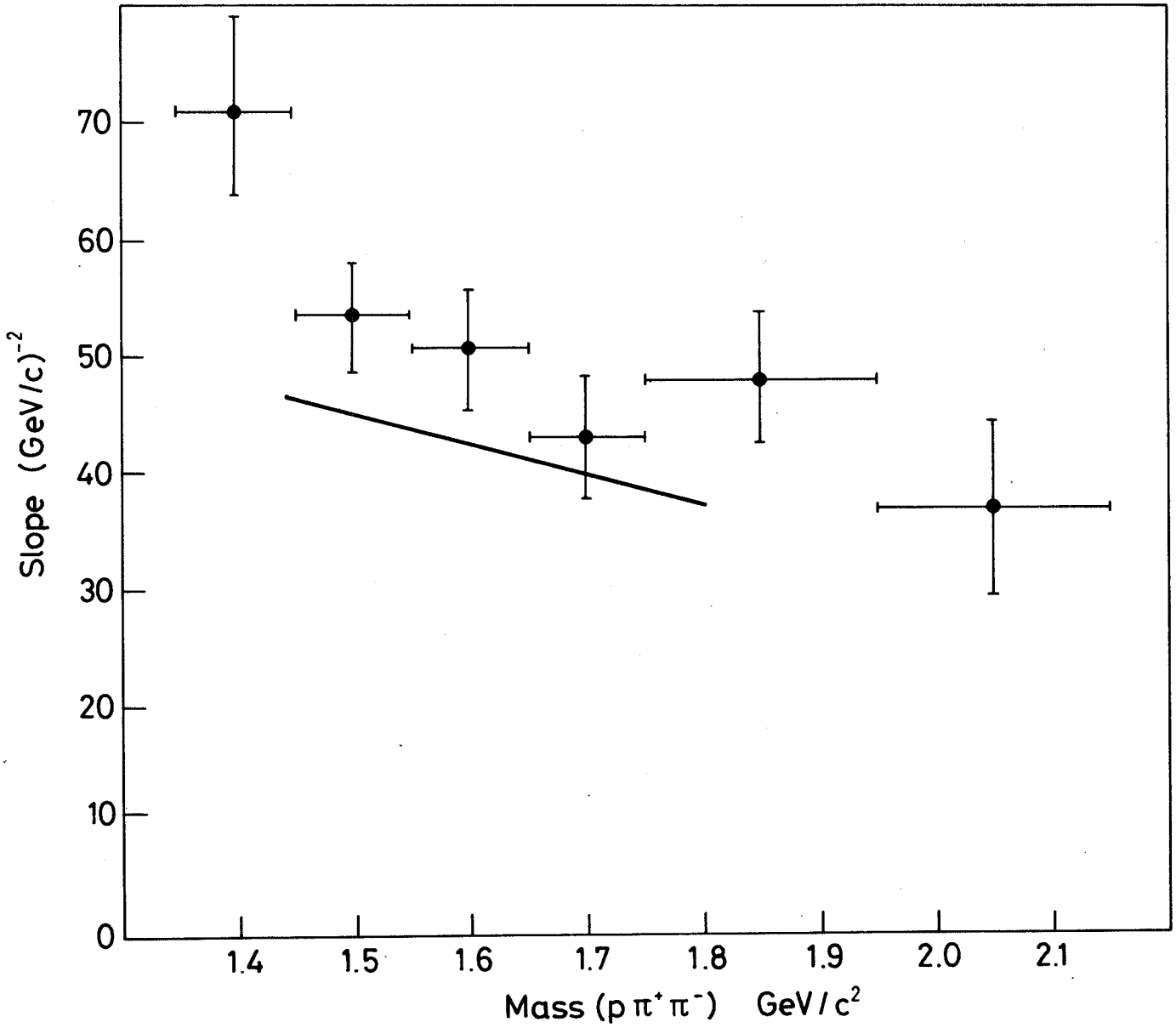
Slope (GeV/c)$^{-2}$
70
60
50
40
30
20
10
0
1.4
1.5
1.6
1.7
1.8
1.9
2.0
2.1
Mass (p π$^+$ π$^-$) GeV/c^2

Fig. 10

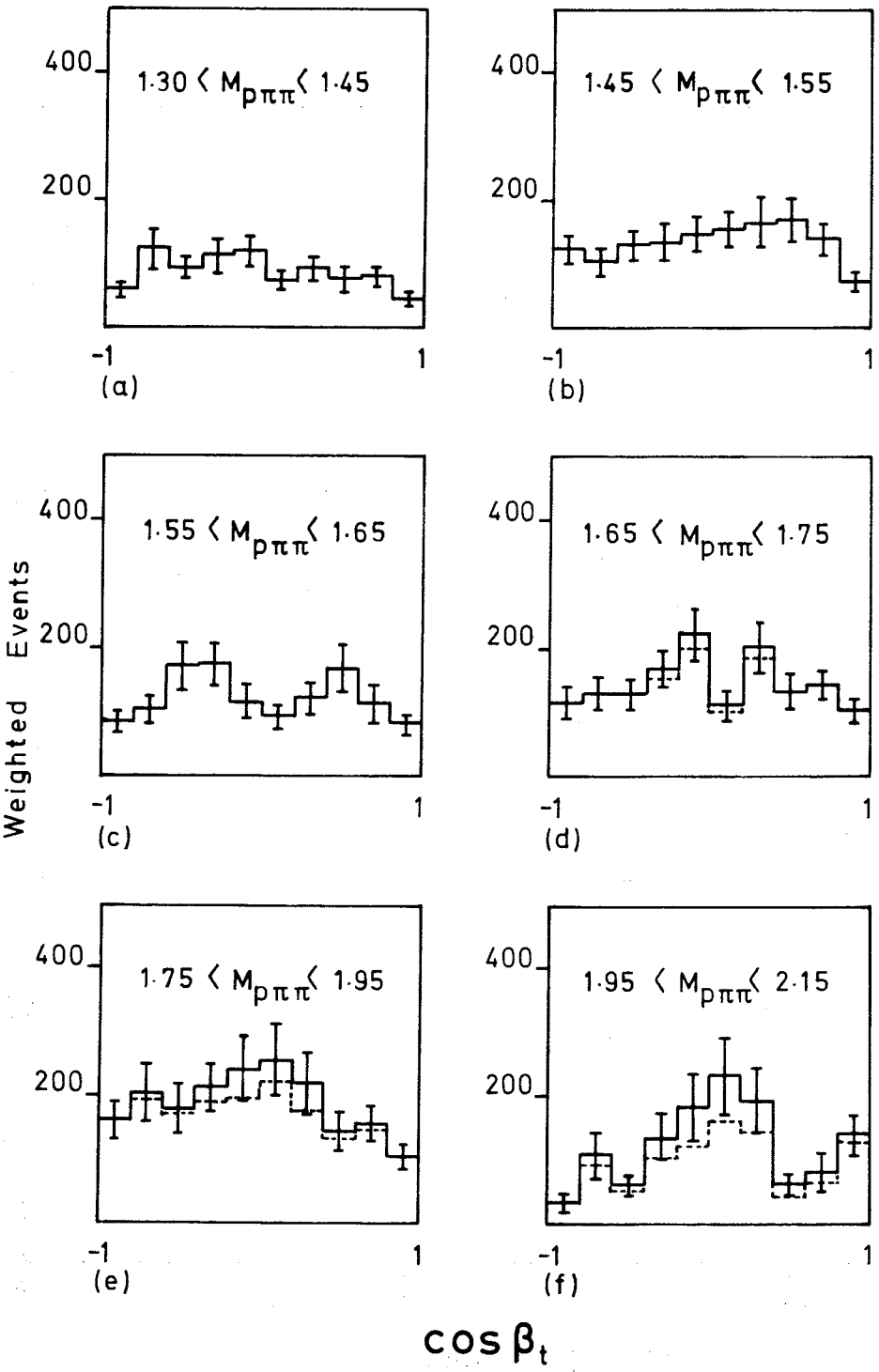
400
200
1·30 < $M_{p\pi\pi}$ < 1·45
-1
1
(a)
1·45 < $M_{p\pi\pi}$ < 1·55
(b)
1·55 < $M_{p\pi\pi}$ < 1·65
(c)
1·65 < $M_{p\pi\pi}$ < 1·75
(d)
1·75 < $M_{p\pi\pi}$ < 1·95
(e)
1·95 < $M_{p\pi\pi}$ < 2·15
(f)
Weighted Events
$\cos\beta_t$

Fig. 11

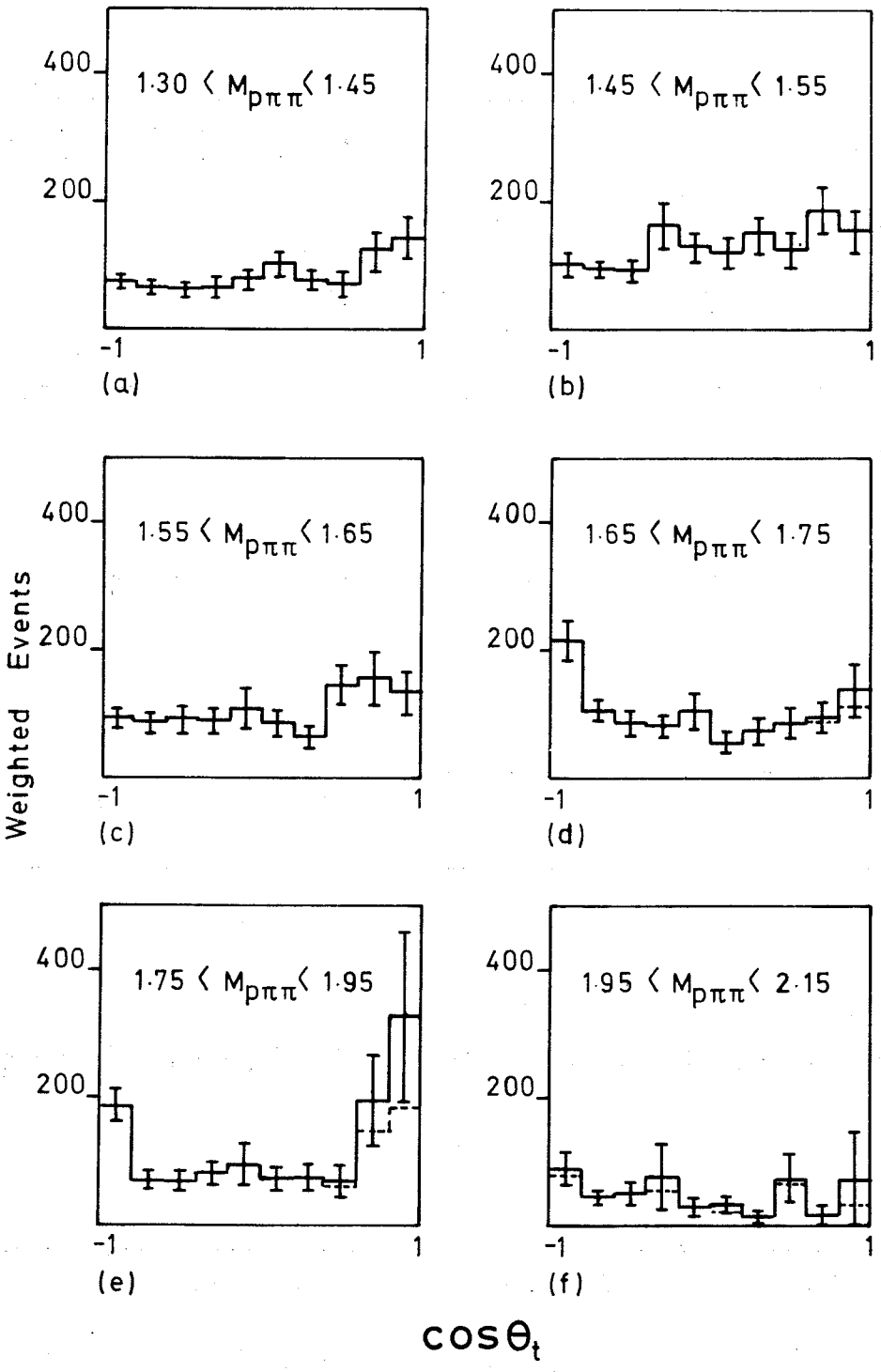
1·30 < Mpππ < 1·45
1·45 < Mpππ < 1·55
1·55 < Mpππ < 1·65
1·65 < Mpππ < 1·75
1·75 < Mpππ < 1·95
1·95 < Mpππ < 2·15
400
200
-1
1
(a)
(b)
(c)
(d)
(e)
(f)
Weighted Events
cosθt

Fig. 12

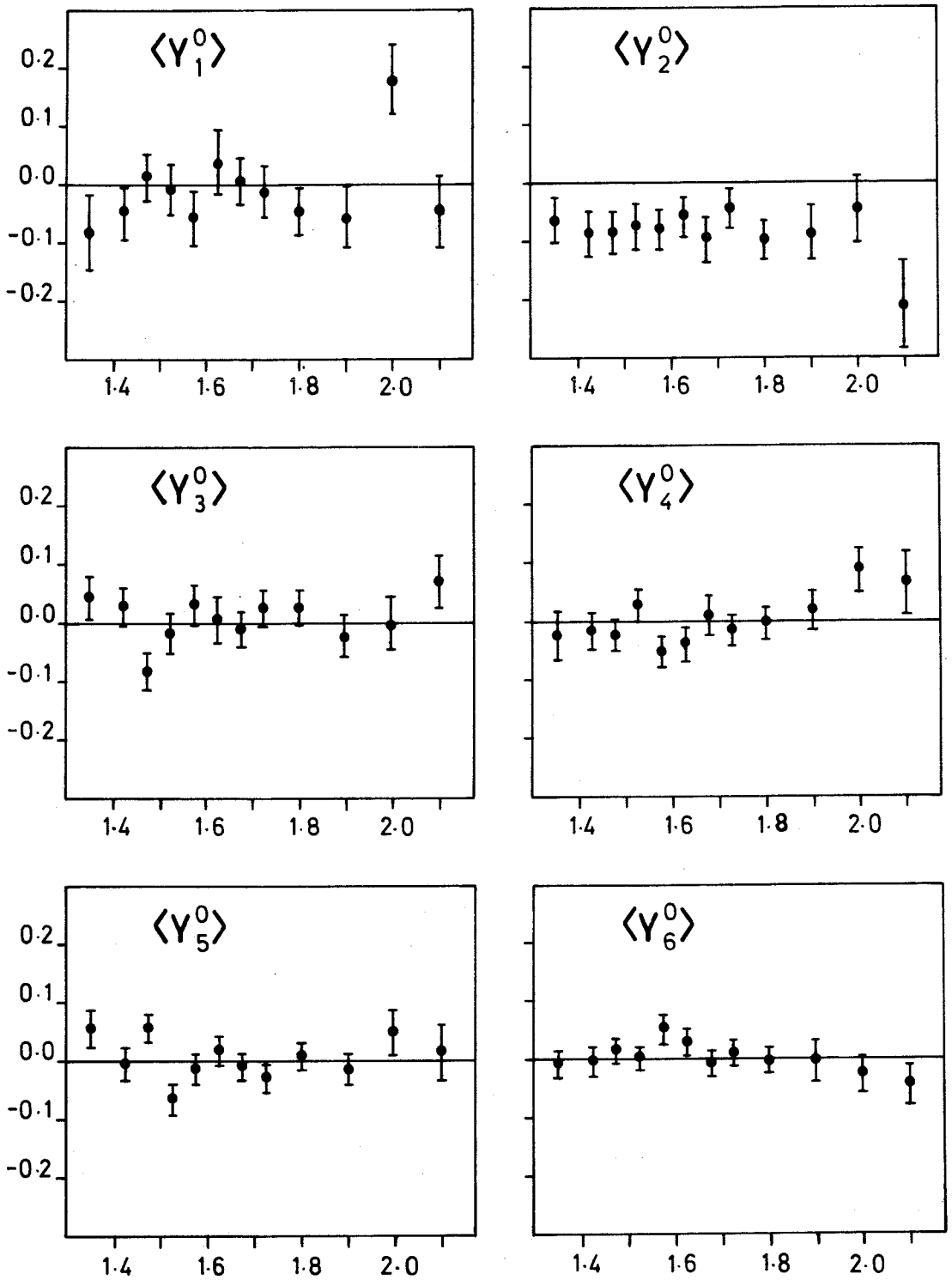

Fig. 13

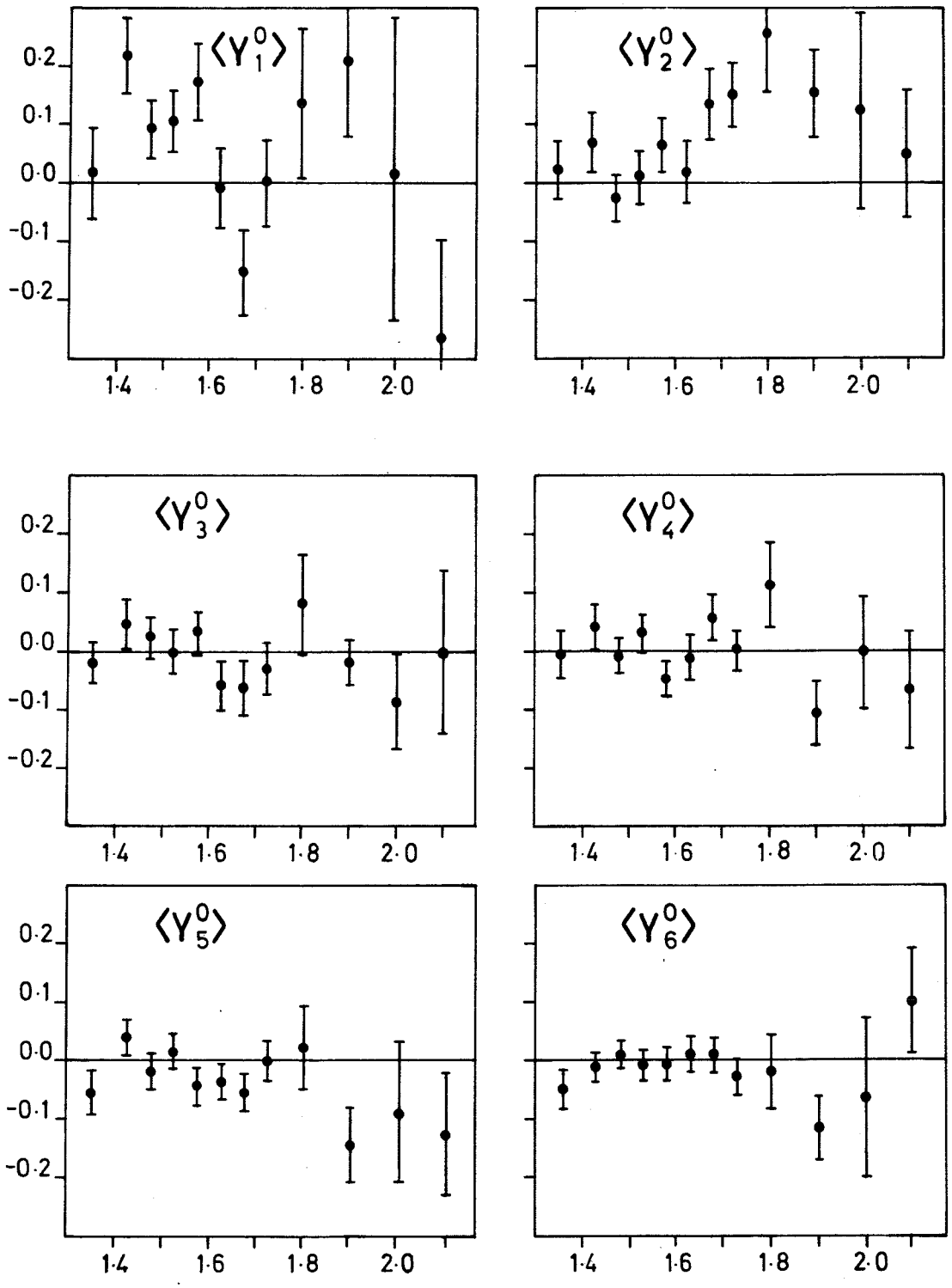
$\langle Y_1^0 \rangle$
$\langle Y_2^0 \rangle$
$\langle Y_3^0 \rangle$
$\langle Y_4^0 \rangle$
$\langle Y_5^0 \rangle$
$\langle Y_6^0 \rangle$
0·2
0·1
0·0
-0·1
-0·2
1·4
1·6
1·8
2·0
Mass ($p\pi^+\pi^-$) GeV/c^2

Fig. 14

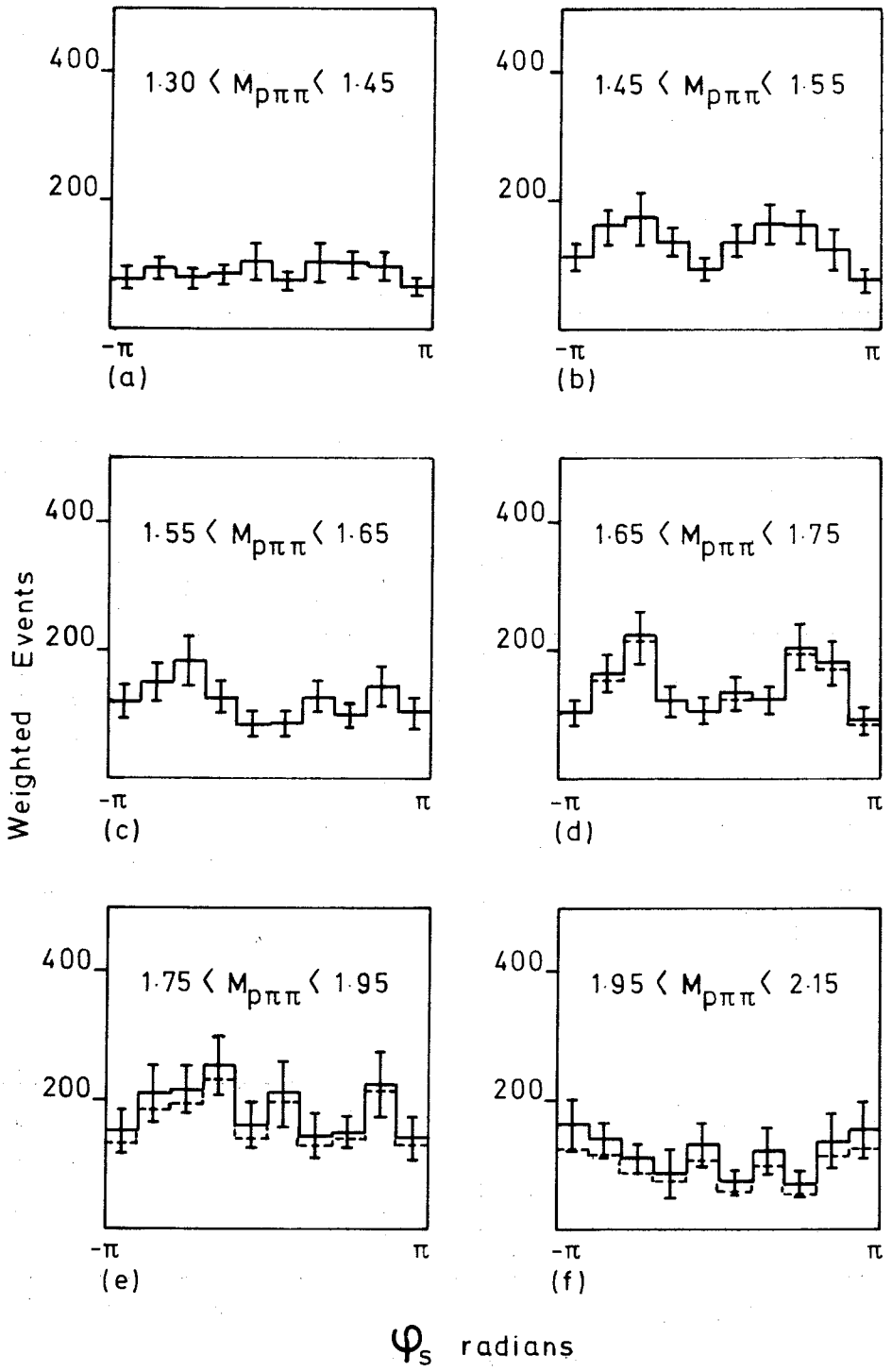
400
200
1·30 < $M_{p\pi\pi}$ < 1·45
-π
π
(a)
1·45 < $M_{p\pi\pi}$ < 1·55
(b)
1·55 < $M_{p\pi\pi}$ < 1·65
(c)
1·65 < $M_{p\pi\pi}$ < 1·75
(d)
1·75 < $M_{p\pi\pi}$ < 1·95
(e)
1·95 < $M_{p\pi\pi}$ < 2·15
(f)
Weighted Events
φ_s radians

Fig. 15

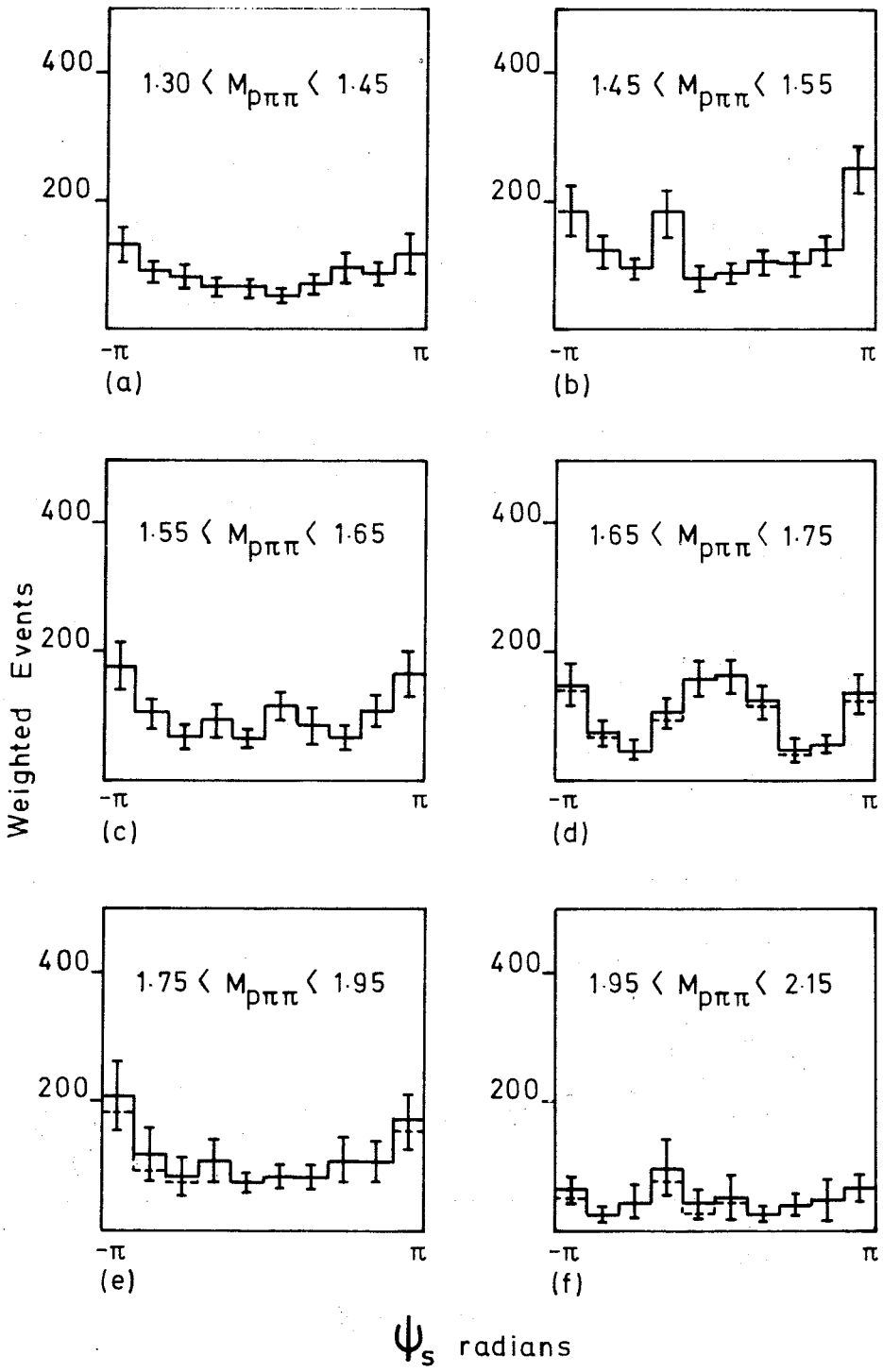
400
200
1·30 < $M_{p\pi\pi}$ < 1·45
-π
π
(a)
1·45 < $M_{p\pi\pi}$ < 1·55
(b)
Weighted Events
1·55 < $M_{p\pi\pi}$ < 1·65
(c)
1·65 < $M_{p\pi\pi}$ < 1·75
(d)
1·75 < $M_{p\pi\pi}$ < 1·95
(e)
1·95 < $M_{p\pi\pi}$ < 2·15
(f)
ψ_s radians

Fig. 16

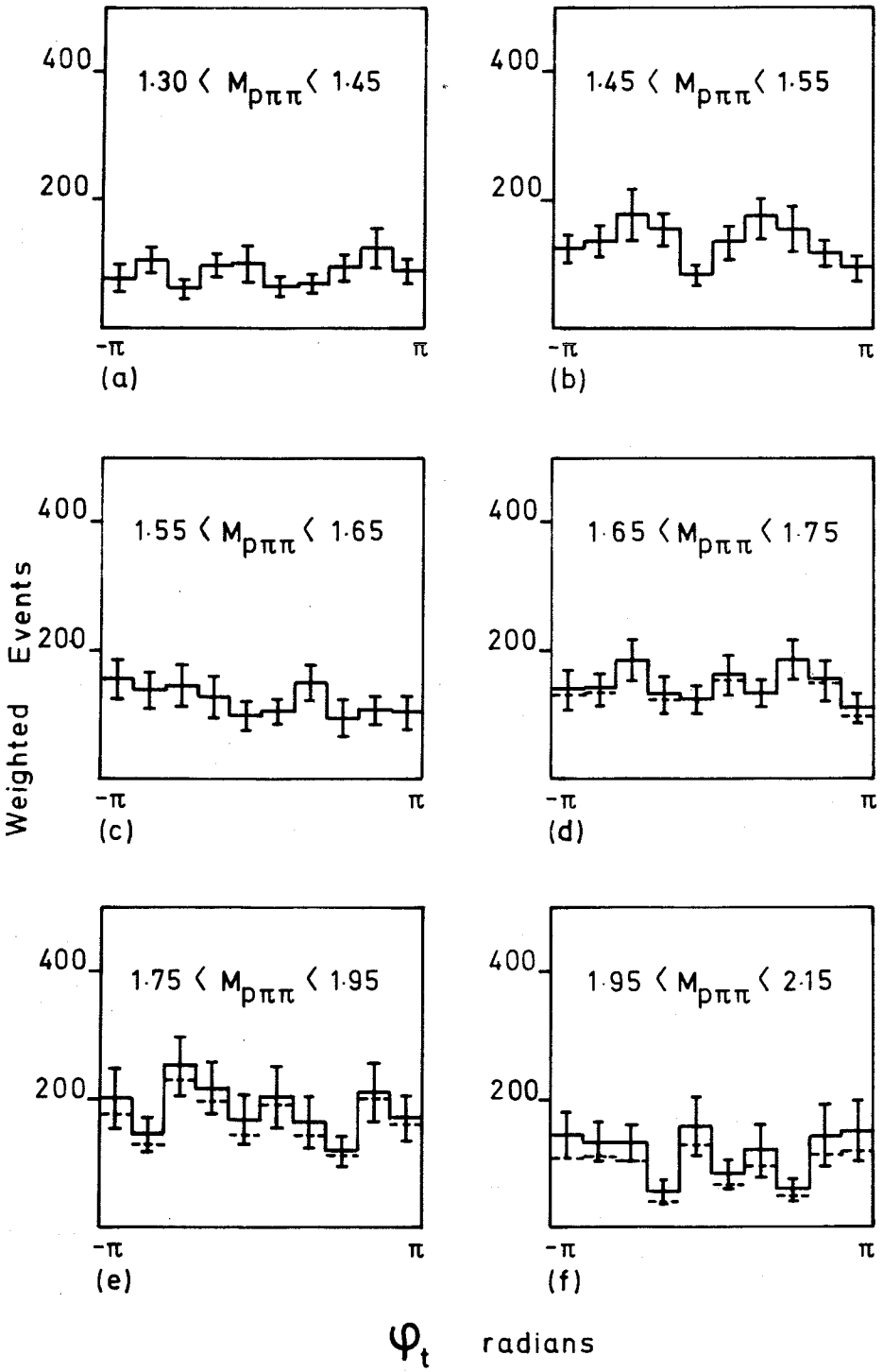
400
200
1·30 < $M_{p\pi\pi}$ < 1·45
-π
π
(a)
1·45 < $M_{p\pi\pi}$ < 1·55
(b)
1·55 < $M_{p\pi\pi}$ < 1·65
(c)
1·65 < $M_{p\pi\pi}$ < 1·75
(d)
1·75 < $M_{p\pi\pi}$ < 1·95
(e)
1·95 < $M_{p\pi\pi}$ < 2·15
(f)
Weighted Events
φ_t radians

Fig. 17

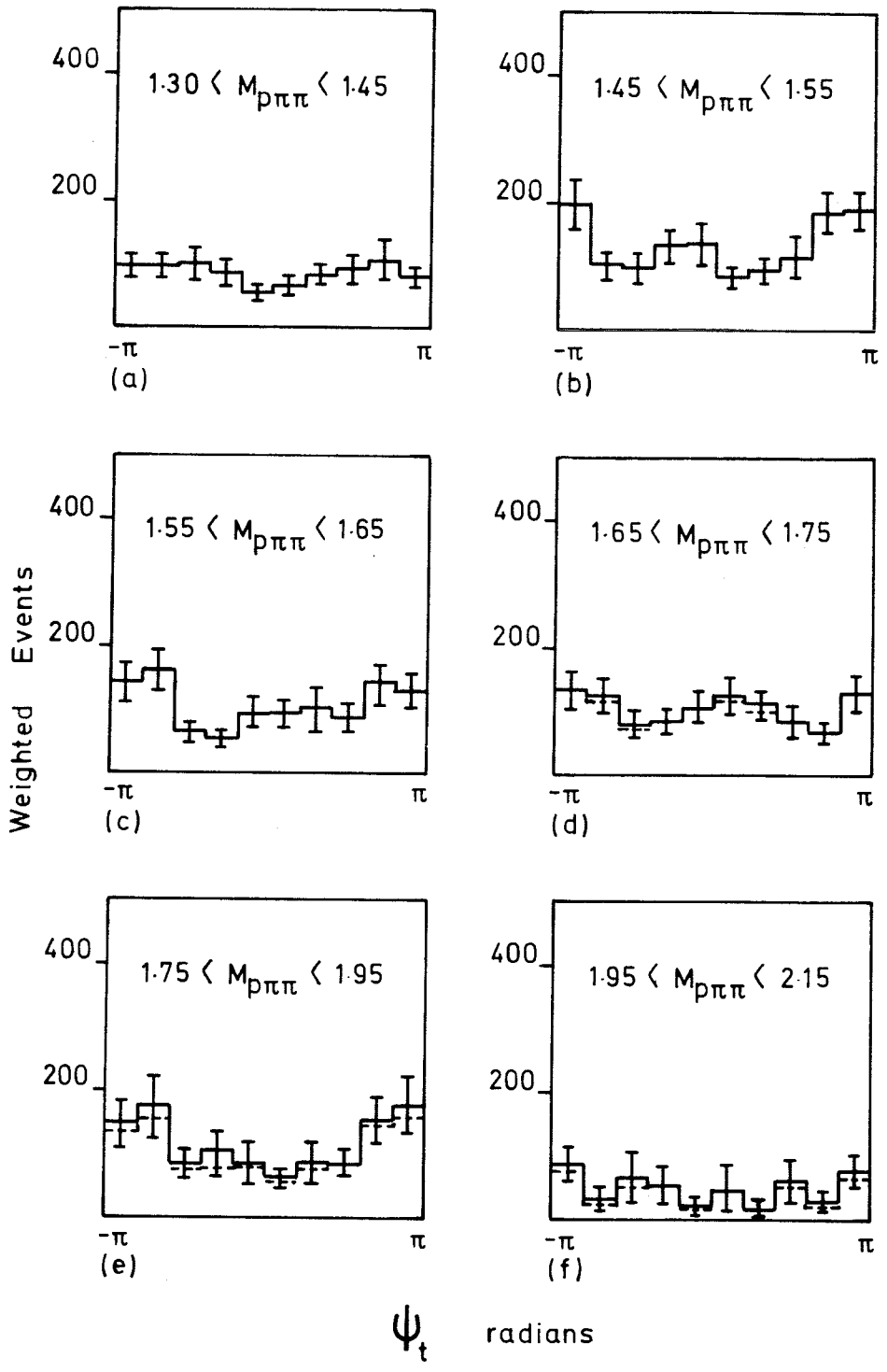
400
200
1·30 < $M_{p\pi\pi}$ < 1·45
-π
π
(a)
1·45 < $M_{p\pi\pi}$ < 1·55
(b)
1·55 < $M_{p\pi\pi}$ < 1·65
(c)
1·65 < $M_{p\pi\pi}$ < 1·75
(d)
1·75 < $M_{p\pi\pi}$ < 1·95
(e)
1·95 < $M_{p\pi\pi}$ < 2·15
(f)
Weighted Events
ψ_t radians

Fig. 18